

Theoretical Analysis of Integrated Nanophotonic Q-Switched Laser Based on Gain and Saturable Absorption by Two-Dimensional Materials

Georgios Nousios,* Thomas Christopoulos, Odysseas Tsilipakos, and Emmanouil E. Kriezis*

A nanophotonic passively Q-switched lasing element in the near infrared is proposed and theoretically investigated. It consists of a silicon-rich nitride disk resonator enhanced with the contemporary MoS₂/WSe₂ hetero-bilayer and a graphene monolayer to provide gain and saturable absorption, respectively. The two-dimensional materials are placed on top of the disk resonator and are separated by a spacer of hexagonal boron nitride. MoS₂/WSe₂ emits at 1128 nm due to the radiative recombination of interlayer excitons after being optically pumped at 740 nm. Optical pumping is conducted in a guided-wave manner aiming at achieving a high overall efficiency by critically coupling to a cavity mode near the pump transition. The response of the proposed pulsed laser is assessed by utilizing a coupled-mode theory framework fed with linear finite-element method simulations, rigorously derived from the Maxwell–Bloch equations. Following a meticulous design process and exploiting the guided pumping scheme, an ultralow lasing threshold of just 24.2 μW is obtained. Overall, the Q-switched laser delivers pulsed light inside an integrated bus waveguide with mW peak power, ps duration, and GHz repetition rates requiring sub-mW continuous wave pumping. These properties are highly promising for communication applications and highlight the potential of two-dimensional materials for nanophotonic light sources.

1. Introduction


Nanophotonic integrated circuits have witnessed immense technological growth over the last two decades and currently constitute the driving force in a number of technological fields including modern-day optical communication systems. In particular, based on the commercial CMOS-compatible and technologically mature silicon-on-insulator (SOI) platform, a number of highly efficient, large-bandwidth, ultra-compact, and low-loss optical components have been demonstrated, including waveguides, resonators, and electro-optic modulators.^[1,2] Recently, the contemporary silicon-rich-nitride-on-insulator (SRNOI) platform, which is complementary (and compatible) to that of SOI, has also attracted great attention.^[3–5] The SRNOI platform combines the high refractive index of Si and the wide bandgap of SiN, allowing for miniaturization and strong light confinement without single- and two-photon-absorption-induced losses and consequent free-carrier effects of Si in

the near infrared (NIR).

Currently, the absence of reliable and efficient SOI-compatible on-chip integrated light sources^[6] constitutes a bottleneck in achieving high-integration-density silicon-based nanophotonic circuitry. Furthermore, exerting control over the laser dynamics through the utilization of an intracavity saturable absorber in order to transform continuous wave (CW) nanophotonic lasers to pulsed sources without the need for external modulation is still vastly unexplored with only one attempt made on photonic crystal cavities recently.^[7] Conventional passive pulsed laser sources exploiting Q-switched and mode-locked mechanisms are rather bulky and typically based on either free-space Fabry–Pérot or fiber-loop cavities, with the gain provided by solid-state and rare-earth-doped fiber lasers, respectively, while the saturable absorption (SA) effect is delivered by semiconductor saturable absorption mirrors (SESAMs).^[8–10] Although the exploitation of the mode-locking mechanism in the nanoscale seems problematic due to the short roundtrip of the nanophotonic cavities, the Q-switching principle seems promising, since it is inherently favored by compact cavity structures.^[8] Nonetheless, bringing the

G. Nousios, T. Christopoulos, E. E. Kriezis
School of Electrical and Computer Engineering
Aristotle University of Thessaloniki (AUTH)
GR-54124 Thessaloniki, Greece
E-mail: gnnousios@ece.auth.gr; mkriezis@auth.gr

O. Tsilipakos
Theoretical and Physical Chemistry Institute
National Hellenic Research Foundation
GR-11635 Athens, Greece

 The ORCID identification number(s) for the author(s) of this article can be found under <https://doi.org/10.1002/adpr.202300249>.

© 2024 The Authors. Advanced Photonics Research published by Wiley-VCH GmbH. This is an open access article under the terms of the Creative Commons Attribution License, which permits use, distribution and reproduction in any medium, provided the original work is properly cited.

DOI: 10.1002/adpr.202300249

Q-switched mechanism in the nanoscale requires novel gain and SA media that could be monolithically integrated with silicon photonic resonators.

The advent of two-dimensional (2D) materials, which exhibit extraordinary linear, nonlinear, and luminescence properties and are compatible with the SOI platform, could help bridge this gap. The first 2D material to be exfoliated was graphene, which is semi-metallic with conical band structure and zero bandgap that gives rise to broadband linear and nonlinear optical properties spanning from the THz into the visible.^[11,12] Graphene saturable absorption was the first nonlinear effect to be studied and then promptly used in pulsed fiber lasers replacing the narrow-band SESAMs.^[13] SA in graphene is characterized by low-power requirements, ultrafast response time and has been thoroughly studied in the literature.^[14–17] The next family of 2D materials that has attracted considerable attention is transition metal dichalcogenides (TMDs), which are semiconductors with a direct bandgap in the visible/NIR and high quantum efficiency, thus holding great promise as active media in nanophotonic lasing elements.^[6,18–23] The vertical stacking of two TMD monolayers creates a type-II band alignment heterostructure hosting interlayer excitons with long radiative recombination lifetime (\approx ns).^[24–30] Additionally, the emission wavelength of the TMD hetero-bilayers depends on the energy levels of the individual monolayers and can be electrically adjusted through the Stark effect.^[24,25,29] MoS₂/WSe₂ is one of the most studied TMD hetero-bilayers which emits in the range 1240–1127 nm (1–1.1 eV), rendering it highly promising for optical communication applications in the lower limit of the O-band.^[29,30] Finally, another promising 2D material for optoelectronic applications is hexagonal boron nitride (h-BN), which is an insulator with wide bandgap of 6 eV and the same crystal structure with graphene.^[31,32] h-BN has been widely used to encapsulate other 2D materials (like graphene and TMDs) in order to enhance their electrical and optical properties and act as gate dielectric in heterostructures of 2D materials.^[31] Recently, exploiting the significant refractive index contrast between h-BN and SiO₂, monolithic devices including disk resonators^[33] and photonic-crystal cavities^[34] have been directly carved out from h-BN flakes (multilayer films up to hundreds of nanometers thick), generating new opportunities for nanophotonic devices fabricated entirely out of 2D materials.

Motivated by the aforementioned developments, in this work we propose, tailor, and thoroughly investigate an integrated passively Q-switched lasing component in the NIR, based on an SRNOI nanophotonic disk resonator where both the gain and SA mechanisms are provided by 2D materials. This is the first time to our knowledge that 2D materials are concurrently used as both gain and SA media in pulsed nanophotonic lasers. Thus far, either various 2D materials (graphene, TMDs, MXenes, black phosphorus) have been employed as saturable absorbers in bulky fiber laser structures^[10] or the gain provided by e.g. TMDs has been exploited in CW nanophotonic lasing elements.^[6,30] Here, the MoS₂/WSe₂ TMD hetero-bilayer is exploited as the gain medium, which emits light at 1128 nm after being optically pumped at 740 nm. In order to minimize the lasing threshold, the gain medium is pumped in a guided-wave manner by appropriately exciting a whispering-gallery mode (WGM) of the cavity near the pump wavelength. The Q-switched operation is achieved

by additionally harnessing the ultrafast SA response of a graphene monolayer. Both the TMD bilayer and graphene monolayer are placed on top of the resonator separated by a finite height spacer of h-BN (multiple layers), allowing for tailoring light-matter interaction between the lasing/pump modes and the gain and SA media. To efficiently excite the pump mode and extract the emitted light from the lasing mode, a double-bus-waveguide scheme is employed with dissimilar waveguides, each of them adjusted to the pump or lasing wavelength. The guided-wave output allows to integrate the proposed source with other optical components on-chip. The cavity is meticulously designed based on general design directives, in order to achieve high-quality performance in terms of pump power requirements, output power, pulse energy and repetition rate.

For designing the proposed lasing element, we develop a rigorous temporal coupled-mode theory (CMT) framework fed by linear finite-element method (FEM) simulations.^[35–41] Both the lasing and pump transitions in the gain medium are described by induced electric polarization fields, which follow typical Lorentzian oscillator equations capable of describing homogeneously broadened transitions.^[36,42–45] The carrier dynamics of the 2D gain medium are described by semiclassical carrier rate equations, while the nonlinear response of graphene by its nonlinear surface conductivity.^[46,47] The effect of the 2D gain and SA media are introduced in the CMT framework exploiting first-order perturbation theory.^[48] Using the developed framework, we thoroughly evaluate both the CW and pulsed operation of the proposed lasing element, in order to quantify all the fundamental emission properties, including the lasing frequency and threshold, the output power and the metrics characterizing the pulsed operation. Finally, the heat removal capability of the structure is assessed by heat transfer simulations,^[49] and its thermal stability is confirmed.

The rest of the paper is summarized as follows: In Section 2, the CMT framework is developed. The photoluminescence and nonlinear properties of the TMD bilayer and graphene monolayer, respectively, are briefly described. In Section 3, the proposed passively Q-switched nanophotonic element is presented and meticulously designed, while in Section 4, both its CW and pulsed operation are thoroughly examined. Finally, Section 5 offers concluding remarks.

2. Theoretical Framework: A Temporal Coupled-mode Theory Approach

2.1. TMD Hetero-bilayer MoS₂/WSe₂ gain

The photoluminescence process of the MoS₂/WSe₂ hetero-bilayer is illustrated in **Figure 1a**, and it is fundamentally the same for every TMD bilayer that forms a type-II band alignment heterostructure.^[24,25,29,30] MoS₂/WSe₂ can be readily modeled as a three-level gain medium,^[41] with levels 1, 2, and 3 being the valence band of WSe₂, the conduction band of MoS₂, and the conduction band of WSe₂, respectively. The surface carrier density in each level is marked as $N_i(\mathbf{r}, t)$, $i = \{1, 2, 3\}$. The pump mode, described by fields $\mathcal{E}^{(p)}(\mathbf{r}, t)$ and $\mathcal{H}^{(p)}(\mathbf{r}, t)$, resonantly excites the A-intralayer excitons of the WSe₂ monolayer. The pump transition is described through the induced pump electric

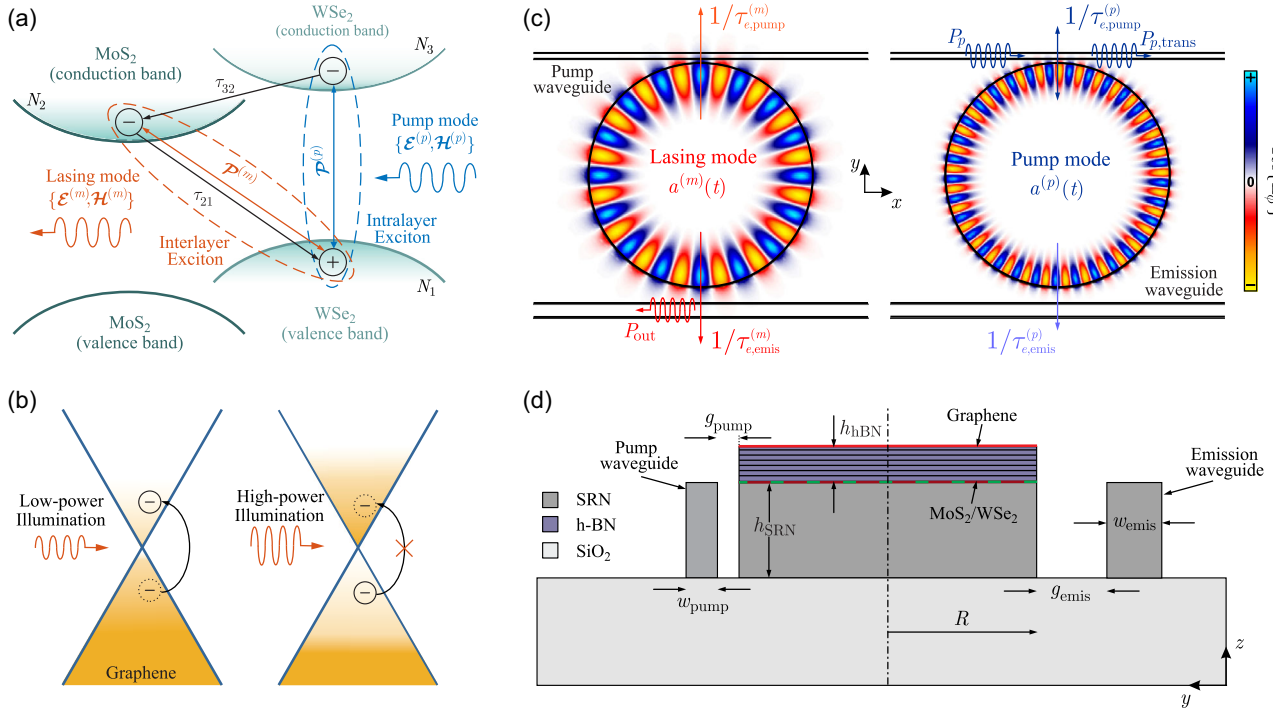


Figure 1. a) Energy diagram of the MoS₂/WS₂ TMD hetero-bilayer, which enables the stimulated emission at 1128 nm due to the radiative recombination of interlayer excitons after being optically pumped at 740 nm. The formation of the interlayer excitons is graphically presented, and all the electromagnetic quantities are marked. b) Graphene band structure and schematic interpretation of the graphene SA effect. c,d) Proposed Q-switched lasing element based on an SRN disk resonator side coupled to two dissimilar bus waveguides. c) Real part of the E_{ϕ} component of both the lasing and pump mode in the TMD plane (x - y cut of the structure). The input and output channels of the two modes are clearly marked including the input and transmitted pump waves and the emitted output wave. d) Schematic of the y - z cut of the structure showing the MoS₂/WS₂/h-BN/graphene stack. All the geometric parameters are annotated.

polarization field $\mathcal{P}^{(p)}(\mathbf{r}, t)$ and is characterized by a central transition wavelength of $\lambda_{31} = 740$ nm (1.675 eV).^[23,29,30] The linewidth of the transition is broad with $\Gamma_{31} \approx 70$ Trads⁻¹ at room temperature.^[20,21] The strength of the transition is quantified by the spontaneous emission lifetime, which has been found to be $\tau_{31,\text{spon}} \approx 290$ ps.^[19,21] In the case of an isolated WS₂ monolayer, the A-intralayer excitons would recombine with the characteristic carrier lifetime τ_{31} , which is in the ps time scale, predominantly dictated by nonradiative channels (at room temperature).^[19,21] Nevertheless, the vertical stacking of the WS₂ and MoS₂ monolayers results in the formation of a type-II band alignment heterostructure leading to the ultrafast carrier transfer of electrons from the conduction band of WS₂ to the empty conduction band of MoS₂, governed by a carrier lifetime τ_{32} in the sub-100 fs time scale;^[24,25] throughout this work we set $\tau_{32} = 100$ fs. At the same time, the recombination of the intralayer excitons of the WS₂ monolayer is quenched^[24,29] and energetically favorable interlayer excitons are formed.^[25,29] The radiative recombination of the interlayer excitons ultimately enables the amplification of the lasing mode $\{\mathcal{E}^{(m)}(\mathbf{r}, t)$ and $\mathcal{H}^{(m)}(\mathbf{r}, t)\}$ from the noise level. The lasing transition is described through the lasing induced polarization field $\mathcal{P}^{(m)}(\mathbf{r}, t)$, and it is characterized by a central transition wavelength of $\lambda_{21} = 1128$ nm (1.1 eV) and a broad linewidth of $\Gamma_{21} \approx 20$ Trads⁻¹.^[29,30] Due to the spatial separation of electrons

and holes in different monolayers, the radiative recombination of the A-interlayer excitons is characterized by spontaneous emission lifetime two orders of magnitude greater than that of the intralayer ones, hence, we set $\tau_{21,\text{spon}} = 25$ ns.^[19,27] The luminescence properties of the interlayer excitons also depend on the twist angle between the two individual monolayers. On that account, the individual TMD monolayers have to be closely aligned crystallographically, enabling the interlayer excitons to recombine radiatively (bright excitons).^[28,29] Nevertheless, to also take into account the various nonradiative recombination channels that may exist, we choose the modest value of $q = 0.1$ for the quantum yield of the interlayer excitons, thus, obtaining a carrier lifetime of $\tau_{21} = 2.5$ ns, in agreement with the value reported in ref. [30]. In addition, we assume that the TMD hetero-bilayer is neutrally doped, where the luminescence is attributed solely to singlet emission with no observation of triplet states.^[28] Note also that since there is no external carrier injection and the gain medium is not chemically active (absence of photobleaching), the total surface carrier density is conserved, i.e., $N_1 + N_2 + N_3 = N_{\text{tot}}$. For the rest of this work, $N_{\text{tot}} = 10^{13}$ cm⁻², which is a typical value for TMDs.^[18] We next proceed to the development of the CMT framework. The 2D nature of the TMD hetero-bilayer dictates that the polarization fields $\mathcal{P}^{(k)}(\mathbf{r}, t)$, $k = \{m, p\}$ contain only tangential components yielding $\mathcal{P}^{(k)}(\mathbf{r}, t) = \mathcal{P}_s^{(k)}(\mathbf{r}, t)\delta_s(\mathbf{r})$, where $\mathcal{P}_s^{(k)}(\mathbf{r}, t)$ is the

surface polarization field (units of C m^{-1}), and $\delta_s(\mathbf{r})$ is a surface Dirac function being nonzero only on the surface of the 2D material. Since the lasing and pump transitions are well separated in frequency and each mode is associated only with one transition, the Maxwell's curl equations for each mode and for nonmagnetic and nondispersive materials read

$$\nabla \times \mathcal{E}^{(k)}(\mathbf{r}, t) = -\mu_0 \frac{\partial \mathcal{H}^{(k)}(\mathbf{r}, t)}{\partial t} \quad (1a)$$

$$\nabla \times \mathcal{H}^{(k)}(\mathbf{r}, t) = \varepsilon_0 \bar{\bar{\epsilon}}_r(\mathbf{r}) \frac{\partial \mathcal{E}^{(k)}(\mathbf{r}, t)}{\partial t} + \frac{\partial \mathcal{P}_s^{(k)}(\mathbf{r}, t)}{\partial t} \delta_s(\mathbf{r}) \quad (1b)$$

where the relative permittivity tensor $\bar{\bar{\epsilon}}_r(\mathbf{r})$ describes the isotropic or uniaxially anisotropic dielectric properties of the underlying bulk materials of the cavity. Note that the polarization fields describe only the resonant nonlinear response due to the respective transition in the gain medium,^[45] while its nonresonant (background) linear dielectric properties are expressed by appropriate imaginary surface conductivity tensors, $\bar{\sigma}$, which can be thought of as contributing to the relative permittivity tensor through the relation $\bar{\bar{\epsilon}}_r = I_3 + j\bar{\sigma}/(\omega\varepsilon_0 d)$, where d is the thickness of the 2D material^[41,46] and I_3 is the 3×3 identity matrix. Throughout this work, the surface conductivity tensors are used for the 2D materials, respecting their two-dimensional nature. The electromagnetic quantities in Equation (1) can be expressed using a complex slowly varying envelope and a rapidly oscillating harmonic term at the optical “carrier” frequency $\Omega^{(k)}$; for instance, the electric field is written as $\mathcal{E}^{(k)}(\mathbf{r}, t) = \text{Re}\{\mathbf{E}^{(k)}(\mathbf{r}, t)\exp(j\Omega^{(k)}t)\}$. The contribution of the complex polarization field $\mathcal{P}_s^{(k)}(\mathbf{r}, t)$ in the respective cavity mode properties is included by exploiting first-order perturbation theory,^[48] i.e., it is assumed that $\mathcal{P}_s^{(k)}(\mathbf{r}, t)$ modifies the resonance frequency and the quality factor of the related mode, but leaves the modal field distribution unaffected. The typical mathematical avenue followed for the incorporation of various linear and nonlinear effects in the CMT framework^[38–40,47,48] is: In the unperturbed case (absence of $\mathcal{P}_s^{(k)}(\mathbf{r}, t)$), the complex fields that fulfill Equation (1) (eigenvectors of a standard eigenfrequency problem) oscillate at the unperturbed/“cold” cavity resonance frequency $\omega_{c,0}^{(k)}$ (subscript “c” stands for “cavity”), i.e., $\Omega^{(k)}$ is set equal to $\omega_{c,0}^{(k)}$. We make no assumption regarding the resonance frequency of each mode and consider the general case where $\omega_{c,0}^{(m)} \neq \omega_{21}$ and $\omega_{c,0}^{(p)} \neq \omega_{31}$, i.e., the resonance frequency of the lasing and pump mode does not necessarily coincide with the central frequency of the respective transition. In the perturbed case (presence of $\mathcal{P}_s^{(k)}(\mathbf{r}, t)$), on the other hand, the complex fields that fulfill Equation (1) oscillate at the perturbed/“hot” cavity resonance frequency $\omega_c^{(k)}$. The evaluation of the resonance frequency shift $\Delta\tilde{\omega}^{(k)} \equiv \omega_c^{(k)} - \omega_{c,0}^{(k)}$, which is generally complex to account for modifications in both the resonance frequency and the linewidth of each mode, is the final objective of the mathematical analysis. There is, however, one notable difference for the lasing mode, where the lasing frequency ω_L (coinciding with the “hot” resonance frequency of the lasing mode, $\omega_c^{(m)}$) is not known a-priori and the CMT framework has to be developed

on an arbitrarily chosen reference frequency $\omega_{\text{ref}}^{(m)}$. The thorough mathematical evaluation of $\Delta\tilde{\omega}^{(m)}$ and a comprehensive discussion on the choice of $\omega_{\text{ref}}^{(m)}$ is presented in our recent work,^[41] while for the extraction of $\Delta\tilde{\omega}^{(p)}$ a similar process has to be followed. Here, we omit the rather long mathematical procedure and present the final result which reads

$$\Delta\tilde{\omega}^{(m)} = j\xi_g^{(m)} \frac{1}{a^{(m)}(t)} \left[j\omega_{\text{ref}}^{(m)} p^{(m)}(t) + \frac{dp^{(m)}(t)}{dt} \right] \quad (2a)$$

$$\Delta\tilde{\omega}^{(p)} = j\xi_g^{(p)} \frac{1}{a^{(p)}(t)} \left[j\omega_{c,0}^{(p)} p^{(p)}(t) + \frac{dp^{(p)}(t)}{dt} \right] \quad (2b)$$

The (solely time-dependent) cavity amplitude $a^{(k)}(t)$ is connected to the slowly varying fields through the relations: $\mathbf{E}^{(k)}(\mathbf{r}, t) = a^{(k)}(t)\mathbf{E}_{\text{ref}}^{(k)}(\mathbf{r})$ and $\mathbf{H}^{(k)}(\mathbf{r}, t) = a^{(k)}(t)\mathbf{H}_{\text{ref}}^{(k)}(\mathbf{r})$.^[41,47] The reference fields $\mathbf{E}_{\text{ref}}^{(k)}(\mathbf{r})$ and $\mathbf{H}_{\text{ref}}^{(k)}(\mathbf{r})$ are proportional to the unperturbed modal field distribution and are normalized in order to have unity energy; the energy of each mode is equal to $|a^{(k)}|^2$. In addition, $p^{(k)}(t)$ is the surface polarization amplitude given by $\mathcal{P}_s^{(k)}(\mathbf{r}, t) = p^{(k)}(t)\mathbf{E}_{\text{ref},\parallel}^{(k)}(\mathbf{r})$, where $\mathbf{E}_{\text{ref},\parallel}^{(k)}(\mathbf{r})$ is the tangential to the 2D gain medium electric field intensity. The latter relation also implies that the induced surface polarization field follows exactly the tangential field distribution of the respective mode.^[36,42] Finally, the overlap factors $\xi_g^{(k)}$ (“g” for “gain”) quantify the strength of interaction between the 2D gain medium and the lasing/pump mode and they are given by

$$\xi_g^{(k)} = \frac{1}{4} \iint_{S_g} |\mathbf{E}_{\text{ref},\parallel}^{(k)}(\mathbf{r})|^2 dS \quad (3)$$

where S_g is the surface of the TMD hetero-bilayer. Note that the definition of $\xi_g^{(k)}$ is different from that of the dimensionless confinement factor of the conventional rate equation framework,^[7,50,51] though both quantities carry the same physical meaning.

The lasing and pump polarization fields follow typical Lorentzian oscillator equations describing homogeneously broadened transitions^[36,43,44] reading

$$\begin{aligned} \frac{\partial^2 \mathcal{P}_s^{(k)}(\mathbf{r}, t)}{\partial t^2} + \Gamma_{iq} \frac{\partial \mathcal{P}_s^{(k)}(\mathbf{r}, t)}{\partial t} + \omega_{iq}^2 \mathcal{P}_s^{(k)}(\mathbf{r}, t) \\ = -\sigma_{iq} \Delta N_{iq}(\mathbf{r}, t) \mathcal{E}_{\parallel}^{(k)}(\mathbf{r}, t) \end{aligned} \quad (4)$$

where the indices $iq = \{31, 21\}$ denote the levels of the gain medium related to each transition. σ_{iq} is the coupling strength of each transition, which is related to the respective spontaneous emission lifetime through $\sigma_{iq} = 3\omega_{iq}\varepsilon_0 n_{\text{gain}}^2 (\lambda_{iq}/n_{\text{gain}})^3 / (4\pi^2 \tau_{iq,\text{spont}})$, where n_{gain} is the refractive index of the gain medium.^[42] The driving term of Equation (4) is the product of the respective mode's electric field and the population difference of the carrier densities of the levels related to the transition, $\Delta N_{iq} \equiv N_i - N_q$. Thus, for $\Delta N_{iq} < 0$ ($\Delta N_{iq} > 0$), Equation (5) describes a saturable absorption (emission) process.

The slowly varying fields are then introduced in Equation (4), with the fields related to the lasing mode/transition oscillating at the reference frequency $\omega_{\text{ref}}^{(m)}$, whereas those related to the pump mode/transition oscillating at the frequency of the input pump wave $\omega^{(p)}$. For instance, the electric field is written as $\mathcal{E}_{\parallel}^{(m)}(\mathbf{r}, t) = \text{Re}\left\{\mathbf{E}_{\parallel}^{(m)}(\mathbf{r}, t)\exp(j\omega_{\text{ref}}^{(m)}t)\right\}$ and $\mathcal{E}_{\parallel}^{(p)}(\mathbf{r}, t) = \text{Re}\left\{\mathbf{E}_{\parallel}^{(p)}(\mathbf{r}, t)\exp(j\omega^{(p)}t)\right\}$. Thereafter, the spatial and temporal dependencies of the fields are disentangled by introducing the reference fields (as previously) and by exploiting the slowly varying envelope approximation to neglect the second-order derivatives, Equations (4) are transformed to

$$\frac{dp^{(m)}}{dt} = -\frac{\omega_{21}^2 - (\omega_{\text{ref}}^{(m)})^2 + j\omega_{\text{ref}}^{(m)}\Gamma_{21}}{\Gamma_{21} + j2\omega_{\text{ref}}^{(m)}}p^{(m)} - \frac{\sigma_{21}}{\Gamma_{21} + j2\omega_{\text{ref}}^{(m)}}[\bar{N}_2 - \bar{N}_1]a^{(m)} \quad (5a)$$

$$\frac{dp^{(p)}}{dt} = -\frac{\omega_{31}^2 - (\omega^{(p)})^2 + j\omega^{(p)}\Gamma_{31}}{\Gamma_{31} + j2\omega^{(p)}}p^{(p)} - \frac{\sigma_{31}}{\Gamma_{31} + j2\omega^{(p)}}[\bar{N}_3 - \bar{N}_1]a^{(p)} \quad (5b)$$

where the temporal dependence has been dropped for brevity. $\bar{N}_i(t)$ are the spatially averaged carrier densities given by

$$\bar{N}_i(t) = \frac{\iint_{S_g} N_i(\mathbf{r}, t) \left| \mathbf{E}_{\text{ref},\parallel}^{(m)}(\mathbf{r}) \right|^2 \left| \mathbf{E}_{\text{ref},\parallel}^{(p)}(\mathbf{r}) \right|^2 dS}{\iint_{S_g} \left| \mathbf{E}_{\text{ref},\parallel}^{(m)}(\mathbf{r}) \right|^2 \left| \mathbf{E}_{\text{ref},\parallel}^{(p)}(\mathbf{r}) \right|^2 dS} \quad (6)$$

The spatial averaging in Equation (6) has to be conducted with the tangential electric fields of both the modes, meaning that when the spatial overlap of the two modes is poor then $\bar{N}_i \approx 0$. Physically, this means that the energy offered by the pump mode cannot be exploited for the amplification of the lasing mode. Inspecting the first term on the right-hand side of Equation (5) and the form of $\Delta\tilde{\omega}$ in Equation (2), we also see that in the general case where $\omega_{\text{ref}}^{(m)} \neq \omega_{21}$ and/or $\omega^{(p)} \neq \omega_{31}$, the polarization amplitudes $p^{(k)}$ induce nonlinear frequency shifts to the resonance frequency of the respective mode.

The carrier densities in the three levels of the gain medium obey standard semiclassical carrier rate equations^[36,43,44] reading

$$\frac{\partial N_3(\mathbf{r}, t)}{\partial t} = \frac{1}{\hbar\omega_{31}}\mathcal{E}_{\parallel}^{(p)}(\mathbf{r}, t) \cdot \frac{\partial \mathcal{P}_s^{(p)}(\mathbf{r}, t)}{\partial t} - \frac{N_3(\mathbf{r}, t)}{\tau_{32}} \quad (7a)$$

$$\frac{\partial N_2(\mathbf{r}, t)}{\partial t} = \frac{1}{\hbar\omega_{21}}\mathcal{E}_{\parallel}^{(m)}(\mathbf{r}, t) \cdot \frac{\partial \mathcal{P}_s^{(m)}(\mathbf{r}, t)}{\partial t} - \frac{N_2(\mathbf{r}, t)}{\tau_{21}} + \frac{N_3(\mathbf{r}, t)}{\tau_{32}} \quad (7b)$$

$$\frac{\partial N_1(\mathbf{r}, t)}{\partial t} = -\frac{1}{\hbar\omega_{21}}\mathcal{E}_{\parallel}^{(m)}(\mathbf{r}, t) \cdot \frac{\partial \mathcal{P}_s^{(m)}(\mathbf{r}, t)}{\partial t} + \frac{N_2(\mathbf{r}, t)}{\tau_{21}} - \frac{1}{\hbar\omega_{31}}\mathcal{E}_{\parallel}^{(p)}(\mathbf{r}, t) \cdot \frac{\partial \mathcal{P}_s^{(p)}(\mathbf{r}, t)}{\partial t} \quad (7c)$$

The first term in Equation (7a) quantifies the photogeneration of intralayer excitons by the pump mode, while the first term in

Equation (7a) and (7c) expresses the stimulated emission (coherent recombination of interlayer excitons) in the lasing mode provided that the population inversion is achieved. The terms $N_3(\mathbf{r}, t)/\tau_{32}$ and $N_2(\mathbf{r}, t)/\tau_{21}$ describe nonradiative and/or incoherent radiative (spontaneous emission) processes that occur from level 3 to level 2 and from level 2 to level 1, respectively (Figure 1a). Note that the relaxation and recombination processes between the different levels of the gain medium are generally nonlinear and could stem from different physical effects.^[52] Here we have chosen to describe them with simple decay terms that depend on constant carrier lifetimes (τ_{21} and τ_{32}), which can be viewed as effective quantities that encapsulate all the underlying nonlinear physical phenomena in an effective manner. More accurate representations using two-electron carrier rate equations have been proposed in the literature,^[53] but we found that they do not lead to noticeable changes in the results presented in Section 4 (see also the Supporting Information, Section S1 for more details and results). By applying the same transformations as previously and additionally exploiting the rotating wave approximation to neglect the second harmonic terms, the (solely time-dependent) rate equations for the spatially averaged carrier densities are found

$$\frac{d\bar{N}_3}{dt} = \frac{\xi_{\text{eff}}^{(p)}}{2\hbar\omega_{31}} \text{Re}\left\{\left[\frac{dp^{(p)}}{dt} + j\omega^{(p)}p^{(p)}\right](a^{(p)})^*\right\} - \frac{\bar{N}_3}{\tau_{32}} \quad (8a)$$

$$\frac{d\bar{N}_2}{dt} = \frac{\xi_{\text{eff}}^{(m)}}{2\hbar\omega_{21}} \text{Re}\left\{\left[\frac{dp^{(m)}}{dt} + j\omega_{\text{ref}}^{(m)}p^{(m)}\right](a^{(m)})^*\right\} - \frac{\bar{N}_2}{\tau_{21}} + \frac{\bar{N}_3}{\tau_{32}} \quad (8b)$$

$$\frac{d\bar{N}_1}{dt} = -\frac{\xi_{\text{eff}}^{(m)}}{2\hbar\omega_{21}} \text{Re}\left\{\left[\frac{dp^{(m)}}{dt} + j\omega_{\text{ref}}^{(m)}p^{(m)}\right](a^{(m)})^*\right\} + \frac{\bar{N}_2}{\tau_{21}} - \frac{\xi_{\text{eff}}^{(p)}}{2\hbar\omega_{31}} \text{Re}\left\{\left[\frac{dp^{(p)}}{dt} + j\omega^{(p)}p^{(p)}\right](a^{(p)})^*\right\} \quad (8c)$$

The overlap factors $\xi_{\text{eff}}^{(k)}$ (not to be confused with the dimensionless confinement factor of the conventional rate equation framework^[7,50,51]) measure the strength of interaction between each mode and the 2D gain medium, as well as the modes between them, and are calculated through (note the different powers in the numerators):

$$\xi_{\text{eff}}^{(m)} = \frac{\iint_{S_g} \left| \mathbf{E}_{\text{ref},\parallel}^{(m)}(\mathbf{r}) \right|^4 \left| \mathbf{E}_{\text{ref},\parallel}^{(p)}(\mathbf{r}) \right|^2 dS}{\iint_{S_g} \left| \mathbf{E}_{\text{ref},\parallel}^{(m)}(\mathbf{r}) \right|^2 \left| \mathbf{E}_{\text{ref},\parallel}^{(p)}(\mathbf{r}) \right|^2 dS} \quad (9a)$$

$$\xi_{\text{eff}}^{(p)} = \frac{\iint_{S_g} \left| \mathbf{E}_{\text{ref},\parallel}^{(m)}(\mathbf{r}) \right|^2 \left| \mathbf{E}_{\text{ref},\parallel}^{(p)}(\mathbf{r}) \right|^4 dS}{\iint_{S_g} \left| \mathbf{E}_{\text{ref},\parallel}^{(m)}(\mathbf{r}) \right|^2 \left| \mathbf{E}_{\text{ref},\parallel}^{(p)}(\mathbf{r}) \right|^2 dS} \quad (9b)$$

2.2. Graphene Saturable Absorption

The realization of a passive Q-switched laser additionally requires harnessing the SA effect. In comparison with other 2D materials, graphene SA is characterized by lower saturation intensity and faster response,^[10] properties that are favorable for the realization of Q-switched laser sources.^[8,9] These SA properties stem from

the unique conical band structure of graphene, which is schematically depicted in Figure 1b.

The linear and nonlinear response of graphene can be treated through its surface conductivity σ_{gr} .^[46] The latter is decomposed into two parts describing the interband and intraband transitions, i.e., $\sigma_{gr} = \sigma_{intra} + \sigma_{inter}$. Due to Pauli blocking, the interband transitions are only allowed when graphene Fermi energy, E_F , is lower than the half-photon energy of the illuminating wave, i.e., $E_F < \hbar\omega/2$. In this regime, the interband component dominates the linear response, and graphene is at the high loss regime. Under strong optical illumination graphene losses are quenched as a result of Pauli blocking. Although both the interband and intraband components of graphene surface conductivity are theoretically anticipated to saturate in the NIR, only the former has been found to occur at practical power densities ($\approx \text{MW cm}^{-2}$).^[12] Therefore, we only consider the saturation of σ_{inter} . We also assume that graphene is pristine ($E_F = 0$), meaning that the intraband losses are zeroed-out ($\sigma_{intra} = 0$), and the linear interband conductivity is purely real and equal to the “universal” optical conductivity of graphene, $\sigma_{inter} = \sigma_0 = 61 \mu\text{S}$.

The SA response of graphene in principle depends on the electric field intensities of both the pump and lasing modes. Nevertheless, to achieve Q-switched lasing, it is crucial that the SA response of graphene remains unaffected by the pump mode; this can be achieved via the careful design of the cavity, which is addressed in Section 3. Otherwise, the losses of graphene would be predominantly saturated by the pump mode (instead of the lasing mode), and the laser could not achieve pulsed operation. The physical description of graphene SA has been treated through a number of different theoretical descriptions in the literature, each of them introducing a different level of physical intuition.^[11,14–16] In all cases, however, the strength of the SA effect can be quantified through a single phenomenological macroscopic parameter, namely, the saturation intensity I_{sat} .^[11,15,17] Additionally, graphene SA has been found to be ultrafast with the SA relaxation time receiving values from 0.1 to 1 ps.^[11,15] Therefore, we opt for a simple instantaneous graphene SA model which, nonetheless, encompasses all the required physical properties that affect the overall response of the Q-switched lasing element. The nonlinear surface conductivity of graphene is given by^[47]

$$\sigma_{gr} \equiv \sigma_{gr}(\mathbf{E}_{||}^{(m)}) = \frac{\sigma_0}{1 + |\mathbf{E}_{||}^{(m)}(\mathbf{r}, t)|^2 / E_{sat}^2} \quad (10)$$

where E_{sat} is the saturation electric field that corresponds to the typical value of the saturation intensity of $I_{sat} = 1 \text{ MW cm}^{-2}$,^[11] they are connected through $I_{sat} = |E_{sat}|^2 / (2Z_0)$ and Z_0 is the vacuum characteristic impedance. Each mode induces a surface current density in the graphene monolayer given by $\mathbf{J}_s^{(k)} = \sigma_{gr} \mathbf{E}_{||}^{(k)}$ where the temporal and spatial dependencies have been dropped for brevity. The impact of $\mathbf{J}_s^{(k)}$ on the properties of the two modes is incorporated once again through first-order perturbation theory, resulting in modifications in the quality factors of the two modes.^[47] Consequently, the graphene SA-induced dynamic lifetime, $\tau_{gr}^{(k)}$, of the two modes is evaluated through

$$\frac{1}{\tau_{gr}^{(k)}(a^{(m)})} = \frac{1}{4} \iint_{S_{SA}} \frac{\sigma_0 |\mathbf{E}_{ref,||}^{(k)}|^2}{1 + |a^{(m)}|^2 |\mathbf{E}_{ref,||}^{(m)}|^2 / E_{sat}^2} dS \quad (11)$$

where S_{SA} is the surface of the saturable absorber, i.e., the graphene monolayer. Equation (11) cannot be further simplified since the solely time-dependent term $|a^{(m)}|^2$ cannot be disentangled from the surface integral. Nevertheless, to gain further physical insight and facilitate the development of design directives (see Section 3), we aim at defining overlap factors similar to $\xi_g^{(k)}$ that express the strength of interaction between the SA and each of the two modes. For this purpose, we set $a^{(m)} = 0$ in Equation (11) and the linear lifetime due to the graphene losses becomes $1/\tau_{gr}^{(k)}(0) = \sigma_0 \xi_{SA}^{(k)}$, with the $\xi_{SA}^{(k)}$ overlap factor given by

$$\xi_{SA}^{(k)} = \frac{1}{4} \iint_{S_{SA}} |\mathbf{E}_{ref,||}^{(k)}(\mathbf{r})|^2 dS \quad (12)$$

Note that Equation (12) is very similar to Equation (3), but the integration is performed on graphene rather than the TMD heterobilayer.

Apart from SA, graphene also possesses strong Kerr effect,^[14,16,54] and in general its impact has to be carefully considered in practical nanophotonic graphene-enhanced structures. Our preliminary calculations indicate that graphene Kerr effect is of negligible importance in our Q-switched lasing element and, thus, its influence is omitted for the rest of this work.

2.3. Overall Cavity Response

Having evaluated the impact of the 2D gain medium [Equation (2)] and the 2D SA [Equation (11)] on the two modes, we are now able to write the final form of the cavity mode amplitude CMT equations. The proposed Q-switched lasing element is comprised of a disk resonator side-coupled to two dissimilar bus waveguides, namely the pump and the emission waveguides. In Figure 1c, we present the field distribution on a x - y cut of the structure for each mode, illustrating the real part of the E_ϕ component of each mode for the designed lasing element (see Section 3). Therein, we also mark the input and output channels as well as the respective external lifetimes. The latter follow the naming convention $\tau_{\epsilon, wg}^{(k)}$, where the subscript $wg = \{\text{emis}, \text{pump}\}$ denotes the waveguide and the superscript marks the mode. The pump waveguide couples the input pump power, P_p , to the resonator in order to excite the pump mode, while the emission waveguide extracts the emitted output power, P_{out} , from the lasing mode. The exploitation of a double-waveguide scheme with dissimilar waveguides is necessary to achieve efficient coupling for both modes, for reasons that will become evident in Section 3. Although the lasing and pump modes are also coupled with the pump and emission waveguide, respectively, these couplings are undesirable and can be minimized in the design stage.

Consequently, the cavity amplitude equation for the lasing mode reads^[41]

$$\begin{aligned} \frac{da^{(m)}}{dt} = & -j\left[\omega_{\text{ref}}^{(m)} - \omega_{c,0}^{(m)}\right]a^{(m)} \\ & - \left[\frac{1}{\tau_{\text{rad}}^{(m)}} + \frac{1}{\tau_{\text{gr}}^{(m)}(a^{(m)})} + \frac{1}{\tau_{e,\text{emis}}^{(m)}} + \frac{1}{\tau_{e,\text{pump}}^{(m)}} \right] a^{(m)} \\ & - \xi_g^{(m)} \left[j\omega_{\text{ref}}^{(m)} p^{(m)} + \frac{dp^{(m)}}{dt} \right] \end{aligned} \quad (13)$$

where the first term on the right-hand side expresses the detuning between the arbitrarily chosen $\omega_{\text{ref}}^{(m)}$ and $\omega_{c,0}^{(m)}$, with any choice of $\omega_{\text{ref}}^{(m)}$ reasonably close to $\omega_{c,0}^{(m)}$ being valid. The actual lasing frequency can be either revealed in a post-processing step by taking the Fourier transform of the evaluated $a^{(m)}$, or estimated through a closed-form relation presented in ref. [41]. The second term is the loaded lifetime of the mode consisting of both power-independent ($\tau_{\text{rad}}^{(m)}$, $\tau_{e,\text{emis}}^{(m)}$ and $\tau_{e,\text{pump}}^{(m)}$) and power-dependent/dynamic ($\tau_{\text{gr}}^{(m)}$) terms; the lifetime is connected to the respective quality factor through $Q^{(k)} = \omega_{c,0}^{(k)} \tau^{(k)}/2$. Finally, the third term introduces the influence of the lasing polarization field in the lasing mode, according to Equation (2a). The output power can be assessed through $P_{\text{out}} = 2/(\tau_{e,\text{emis}}^{(m)})|a^{(m)}|^2$.

Similarly, the cavity amplitude equation for the pump mode can be cast as

$$\begin{aligned} \frac{da^{(p)}}{dt} = & -j\left[\omega^{(p)} - \omega_{c,0}^{(p)}\right]a^{(p)} \\ & - \left[\frac{1}{\tau_{\text{rad}}^{(p)}} + \frac{1}{\tau_{\text{gr}}^{(p)}(a^{(p)})} + \frac{1}{\tau_{e,\text{emis}}^{(p)}} + \frac{1}{\tau_{e,\text{pump}}^{(p)}} \right] a^{(p)} \\ & - \xi_g^{(p)} \left[j\omega_{c,0}^{(p)} p^{(p)} + \frac{dp^{(p)}}{dt} \right] + j\sqrt{\frac{2}{\tau_{e,\text{pump}}^{(p)}}} \sqrt{P_p} \end{aligned} \quad (14)$$

where the fourth term is the driving term, i.e., the input wave that excites the pump mode. Pump power that is transmitted in the pump waveguide is $P_{p,\text{trans}} = \left| \sqrt{P_p} + j\sqrt{2/\tau_{e,\text{pump}}^{(p)}} a^{(p)} \right|^2$, while the pump power transmitted/dropped in the emission waveguide is negligible in the designed structure. We also define the absorption efficiency η_p of the laser as the fraction of the input pump power P_p that it is absorbed by the gain medium (and more specifically the WSe₂ monolayer). Under the reasonable approximations that the radiative losses, the coupling losses with the emission waveguide and the graphene resistive losses are negligible, the absorption efficiency can be calculated through $\eta_p = (P_p - P_{p,\text{trans}})/P_p$.

The final CMT framework consists of Equation (5), (8), (13) and (14) (and the respective output power-coupling equations), which comprise a system of seven fully-coupled nonlinear first-order differential equations and have to be solved in conjunction with each other in order to assess the response of the lasing element under study. The coefficients of the CMT differential equations can be evaluated by conducting linear eigenfrequency simulations using a full-wave electromagnetic method. The framework can be exploited to assess the response of a general “class C” laser, where the carrier dynamics and the

polarization response of the gain medium are considered to determine the overall response of the laser. In comparison with our recent work,^[41] here we have expanded the CMT framework to incorporate the case where the optical pumping is conducted with a tightly confined cavity mode excited by guided light rather than a uniform free-space beam. In addition, the SA effect has been introduced in the framework enabling the study of pulsed nanophotonic lasing structures. Moreover, the pump transition is now described through an electric polarization field, similarly to the lasing transition, enabling the accurate evaluation of the pump light absorption by the gain medium, including the saturation of the pump transition at high pump power levels due to Pauli blocking. The biggest advantage of the guided pumping scheme is the prospect of achieving absorption efficiency, $\eta_p \rightarrow 1$, which has far-reaching consequences for nanophotonic lasing elements as it could result in the ultralow lasing thresholds in the μW region. Maximum absorption efficiency can be attained by appropriately designing the resonator in order to meet a typical critical coupling condition for the pump mode.

The onset of the lasing operation is quantitatively described through the lasing threshold, which can be expressed either through the population inversion threshold or the corresponding pump power threshold. The population inversion threshold can be readily extracted from Equation (13) in the specific case that $\omega_{\text{ref}}^{(m)} = \omega_{c,0}^{(m)} = \omega_{21} \equiv \omega_L$ yielding: $\Delta\bar{N}_{21,\text{th}}^{(1)} = \Gamma_{21}/[\sigma_{21}\xi_g^{(m)}\tau_\ell^{(m)}(0)]$, where $\tau_\ell^{(m)}(0)$ is the linear loaded lifetime of the lasing mode.^[41] Lasing operation could then be achieved provided that $\Delta\bar{N}_{21,\text{th}}^{(1)} < N_{\text{tot}}$. This threshold is also marked with the superscript “(1)” denoting the “first” lasing threshold, i.e., the population inversion required to compensate the (linear) losses experienced by the lasing mode. The onset of the Q-switched (pulsed) operation can also be revealed by a similar condition, which is commonly referred to as the “second threshold condition” or Q-switch condition and expresses whether or not a cavity with gain and SA can achieve pulsed operation.^[8,9,42] A qualitative description to the Q-switch condition can be given as follows: For pump power levels above the first lasing threshold, a population inversion is developed leading to the amplification of the lasing mode with the small-signal gain coefficient. Following this initial growth rate, a Q-switched pulse would develop provided that the saturation of the SA medium occurs before the saturation of the initial population inversion.^[42] The saturation of the gain and SA media are related to their intrinsic physical properties and their overlap with the lasing mode. The long radiative recombination lifetime of MoS₂/WSe₂ and the low saturation intensity of graphene inherently favors the fulfillment of the second threshold condition.^[8,9] Nonetheless, to obtain Q-switched operation the cavity structure should be appropriately designed for the overlap of the lasing mode with the SA medium to be strong and comparable to that between the lasing mode and the gain medium. Quantitatively, the “second threshold condition” can be expressed through the second population inversion threshold $\Delta\bar{N}_{21,\text{th}}^{(2)}$, which can be evaluated from our CMT framework (Equation (5), (8), (13), and (14)) through a number of approximations following the procedure described in ref. [42]. The accuracy of $\Delta\bar{N}_{21,\text{th}}^{(2)}$ to predict the Q-switch operation is typically good provided that the pump mode has

negligible impact on the carrier dynamics and therefore on the output emitted pulses. Our preliminary assessments, however, have revealed that this is not the case for the three-level gain medium with the guided-wave pumping under study.

3. Physical Structure

As it has been briefly described in Section 2.3, the proposed structure consists of a disk resonator side coupled to two dissimilar bus waveguides, with x - y and y - z cuts of the structure schematically presented in Figure 1c,d. All the geometric parameters of the configuration are marked in Figure 1d. In this section, we design the physical structure for optimum performance. We will initially focus on the uncoupled cavity, followed by the full structure.

The silicon-rich nitride (SRN) disk resonator of radius R and height h_{SRN} supports tightly confined, high-Q-factor whispering-gallery modes (WGMs) favorable for the realization of low threshold lasing elements. SRN has a bandgap of 2.05 eV (605 nm);^[4] thus, one-photon absorption is prohibited at both the lasing and pump wavelengths. Such resistive losses would impede the lasing process by increasing the lasing threshold, while also increasing the Joule-generated heat in the cavity (see also Section 4 and the Supporting Information, Section S4). Note that both wavelength regions of interest are beyond the two-photon absorption (TPA) bandgap (corresponds to a wavelength of 1210 nm), where SRN has been found to have TPA coefficients of $\beta_{\text{TPA}} \approx 10^{-10} \text{ mW}^{-1}$.^[5] TPA can be introduced in the CMT framework with appropriate nonlinear lifetimes,^[37] similarly to the handling of graphene SA effect (Equation (11)). The impact of TPA on the response is found to be negligible for the pump power levels examined in Section 4, and thus it has been omitted in this work. Similar conclusions can be drawn for the Kerr effect in SRN, which is characterized by a nonlinear refractive index of $n_2 \approx 10^{-17} \text{ m}^2\text{W}^{-1}$.^[5] The refractive index of SRN in the lasing wavelength region ($\lambda \approx \lambda_{21}$) is $n_{\text{SRN}} = 3.15$, whereas in the pump wavelength region ($\lambda \approx \lambda_{31}$) $n_{\text{SRN}} = 3.36$.^[4] The refractive index of SiO_2 in both wavelength regions is $n_{\text{SiO}_2} = 1.45$. The TMD hetero-bilayer and the graphene monolayer are patterned in disks matching the resonator and placed on top of it, separated by a finite-height spacer of h-BN with height equal to h_{hBN} (see Figure 1d). Owing to its layered nature, h-BN multilayer films are uniaxially anisotropic materials experiencing different in-plane (n_{\parallel}) and out-of-plane (n_{\perp}) refractive indices.^[32] More specifically, for $\lambda \approx \lambda_{21}$, the refractive indices of h-BN are $n_{\text{hBN},\parallel} = 2.1$ and $n_{\text{hBN},\perp} = 1.82$, while for $\lambda \approx \lambda_{31}$ we have $n_{\text{hBN},\parallel} = 2.12$ and $n_{\text{hBN},\perp} = 1.84$. We also have to consider the nonresonant (background) linear dielectric properties of the two TMD monolayers, as discussed in Section 2.1. In the lasing wavelength region, the surface conductivity of the bilayer is $\sigma_{\text{bilayer}} = j369 \mu\text{S}$,^[22,41] while in the pump wavelength region, we have $\sigma_{\text{bilayer}} = j573 \mu\text{S}$.^[23,41] To calculate the coupling strengths, σ_{12} and σ_{31} , we use $n_{\text{gain}} \approx 4.5$,^[22,23] yielding $\sigma_{21} = 1.43 \times 10^{-8} \text{ C}^2\text{kg}^{-1}$ and $\sigma_{31} = 5.32 \times 10^{-7} \text{ C}^2\text{kg}^{-1}$.

The role of the h-BN layer in our cavity is twofold. First, it provides the necessary electrical isolation between the TMD bilayer and graphene monolayer. Even more importantly, its finite

height provides an invaluable degree of freedom in order to tailor each mode's overlap with $\text{MoS}_2/\text{WSe}_2$ and graphene. Specifically, the disk geometric parameters (R , h_{SRN} and h_{hBN}) have to be appropriately selected in order to result in equally strong overlap between the lasing mode and both $\text{MoS}_2/\text{WSe}_2$ and graphene. The latter is essential for obtaining Q-switched operation according to the qualitative discussion regarding the second threshold condition in Section 2.3. This constitutes the *first design directive*, and it can be mathematically expressed as $\xi_{\text{g}}^{(m)}/\xi_{\text{SA}}^{(m)} \leq 3.5 \text{ dB}$, meaning the two ξ factors should be of the same order of magnitude. Note that ξ factors expressing the overlap between the two modes and $\text{MoS}_2/\text{WSe}_2$ are always greater than those describing the respective modal overlap with graphene, due to the relative position of the two sheets (see Figure 1d). At the same time, the choice of R , h_{SRN} , and h_{hBN} needs to ensure a weak overlap between the pump mode and graphene, in contrast to the overlap between the pump mode and $\text{MoS}_2/\text{WSe}_2$ which should be large to favor pump absorption. This is crucial so that the saturation of loss stems only from the lasing mode (see Section 2.2), as reflected by Equation (10). This is the *second design directive* and it is quantified through $\xi_{\text{g}}^{(p)}/\xi_{\text{SA}}^{(p)} \geq 10 \text{ dB}$, meaning that $\xi_{\text{g}}^{(p)}$ should acquire a value at least an order of magnitude greater than $\xi_{\text{SA}}^{(p)}$. Lastly, the selected parameters have to provide equally strong overlap between the TMD bilayer and both lasing and pump modes in order to achieve low lasing threshold and efficient pumping. This is the *third design directive*, and it is quantified by $\xi_{\text{g}}^{(m)}/\xi_{\text{g}}^{(p)} \leq 3.5 \text{ dB}$, meaning that the two ξ factors should be of the same order of magnitude. The fulfillment of these three design directives is inherently favored in our structure since the refractive index contrast of SRN and h-BN results in the lasing mode (corresponds to the longer wavelength) to be equally confined in both SRN and h-BN layers, while the pump mode (corresponds to the shorter wavelength) confined predominantly in the higher index material, i.e., inside SRN.

To obtain the optimum geometric parameters of the disk resonator, we conduct electromagnetic full-wave eigenfrequency simulations for the uncoupled disk resonator using the 2D axisymmetric module of COMSOL Multiphysics. The parametric simulations were conducted by varying the h_{SRN} and h_{hBN} in the practical height intervals of 200–300 nm and 20–130 nm, respectively. The azimuthal order of the lasing mode is kept constant and equal to $m = 16$, while for each h_{SRN} and h_{hBN} value, the radius R is tuned in order to achieve $\lambda_{c,0}^{(m)} = \lambda_{21}$. This is necessary in order to allow for the maximum possible amplification for the lasing mode. Note that the azimuthal order of the lasing mode has a less pronounced impact on the ξ factors than the height of the disk resonator.^[41] The WGM closer to λ_{31} is used as the pump mode. Although $\lambda_{c,0}^{(p)}$ is in general different from λ_{31} , the lasing operation is not at all hindered, since the pump transition linewidth is very broad ($\Gamma_{31} = 70 \text{ Trads}^{-1}$, corresponding to 20.35 nm), and maximum absorption efficiency ($\eta_p \rightarrow 1$) can be always achieved provided that the appropriate critical coupling condition is met. For the examined values of h_{SRN} and h_{hBN} , we can always obtain a WGM with resonance wavelength within 10 nm from λ_{31} and practically infinite radiative quality factor

($Q_{\text{rad}}^{(p)} \approx 10^9$). Note that as h_{SRN} and h_{hBN} change, the azimuthal order of the obtained pump mode is not constant, varying from $m = 31$ to $m = 36$. The emerging results for the ratios $\xi_g^{(m)}/\xi_{\text{SA}}^{(m)}$, $\xi_g^{(p)}/\xi_{\text{SA}}^{(p)}$, and $\xi_g^{(m)}/\xi_g^{(p)}$ in the $h_{\text{SRN}}-h_{\text{hBN}}$ parameter space are presented in **Figure 2a–c**. The ratios $\xi_g^{(m)}/\xi_{\text{SA}}^{(m)}$ and $\xi_g^{(p)}/\xi_{\text{SA}}^{(p)}$ are mainly determined by h_{hBN} and remain almost unaffected by h_{SRN} . The fulfillment of the first design directive requires low values of h_{hBN} , whereas for the second design directive we need high values of h_{hBN} . Finally, the ratio $\xi_g^{(m)}/\xi_g^{(p)}$ mainly depends on h_{SRN} , and the third design directive is favored by low values.

The radiative quality factor of the lasing mode also varies greatly in the $h_{\text{SRN}}-h_{\text{hBN}}$ plane and covers a span of three orders of magnitude (**Figure 2d**). $Q_{\text{rad}}^{(m)}$ drops as h_{SRN} decreases, since the lasing mode leaks more outside the disk. High radiative losses for the lasing mode could hinder the lasing process by increasing the (first) lasing threshold and, even more crucially, by excessively increasing the coupling losses with the pump waveguide, as it will become obvious below. For this purpose, we set a *fourth design directive* demanding that the lasing mode is tightly confined inside the cavity, and its radiative quality factor obtains values $Q_{\text{rad}}^{(m)} > 100\,000$. We have to set an additional

fifth design directive that concerns the overall coupled disk resonator, demanding $\Delta\bar{N}_{21,\text{th}}^{(1)}/N_{\text{tot}} < 1$ so that the lasing process can start. $\Delta\bar{N}_{21,\text{th}}^{(1)}/N_{\text{tot}}$ is depicted in the $h_{\text{SRN}}-h_{\text{hBN}}$ plane in **Figure 2e** and has been evaluated for the typical values of $Q_{e,\text{emis}}^{(m)} = 3\,000$ and $Q_{e,\text{pump}}^{(m)} = 10\,000$. We conclude that the fifth design directive is satisfied for almost every combination of the two heights of the resonator, except for very low values of h_{hBN} where the high linear resistive losses of graphene prohibit lasing. The white quadrilateral area in **Figure 2e** indicates the region where all the five design directives are concurrently fulfilled. Therefore, we choose $h_{\text{SRN}} = 240$ nm and $h_{\text{hBN}} = 70$ nm, with the selected point marked with a star in the maps of **Figure 2**. The exact disk radius for the selected heights is $R = 1.4578$ μm , and the azimuthal order of the pump mode is $m = 33$.

For the selected geometric parameters of the uncoupled resonator, we plot the tangential to the 2D materials electric field of the two modes in **Figure 2f,g**, visually confirming that we have obtained the desired overlap properties between the modes and the 2D gain and SA materials. The real part of the E_ϕ component of the two modes in the TMD plane is depicted in **Figure 1c**. Note also that we have single-mode operation in our proposed lasing

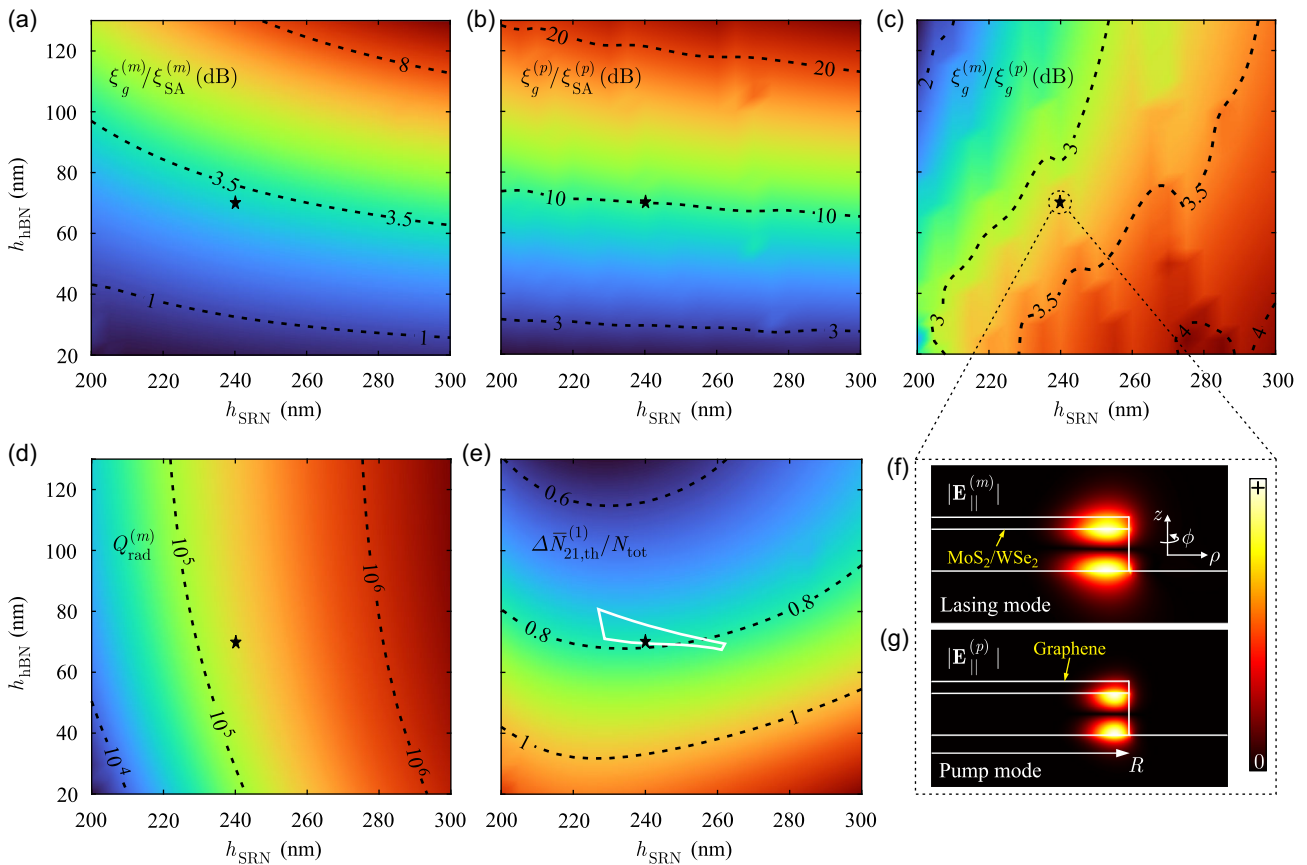


Figure 2. Variation of the CMT parameters: a) $\xi_g^{(m)}/\xi_{\text{SA}}^{(m)}$, b) $\xi_g^{(p)}/\xi_{\text{SA}}^{(p)}$, c) $\xi_g^{(m)}/\xi_g^{(p)}$, d) $Q_{\text{rad}}^{(m)}$, and e) $\Delta\bar{N}_{21,\text{th}}^{(1)}/N_{\text{tot}}$ in the $h_{\text{SRN}}-h_{\text{hBN}}$ plane. The quantities in (a–c) are expressed in dBs. $\Delta\bar{N}_{21,\text{th}}^{(1)}/N_{\text{tot}}$ in panel (e) has been calculated for $Q_{e,\text{emis}}^{(m)} = 3\,000$ and $Q_{e,\text{pump}}^{(m)} = 10\,000$. The white contour in (e) indicates the region where all five design directives are concurrently fulfilled, while the selected point $\{h_{\text{SRN}}, h_{\text{hBN}}\} = \{240$ nm, 70 nm $\}$ is marked with a star. f,g) Norm of the tangential to the 2D materials electric field of the (f) lasing and (g) pump mode in the $x = 0$ plane for the finally selected $\{h_{\text{SRN}}, h_{\text{hBN}}\}$ point.

structure,^[41] since the neighboring-to-the-lasing-mode WGMs are located at 1 170.85 nm ($m = 15$) and 1 088.5 nm ($m = 17$), thus, well outside the emission Lorentzian of $\Gamma_{21} = 20 \text{ Trads}^{-1}$ (13.5 nm) (see Supporting Information, Section S2 for more details and results on the design process).

We can now proceed to determine the coupling gaps of the double bus-waveguide configuration. The necessity for using two dissimilar waveguides originates from the large spectral distance between the lasing and pump modes. As a result, the radiative quality factors $Q_{\text{rad}}^{(k)}$ of the two modes differ by many orders of magnitude (see Table 1), making the efficient coupling with a single-waveguide scheme quite challenging. The two waveguides have equal heights with the SRN disk resonator, and their widths (w_{emis} and w_{pump}) are appropriately determined for single-mode operation in each wavelength region of interest. To this end, we set $w_{\text{emis}} = 180 \text{ nm}$ and $w_{\text{pump}} = 80 \text{ nm}$. The supported mode is the TM_{00} , which is the lowest order quasi-TM mode with E_z being the dominant transverse electric field component. The bus waveguides are side coupled to the disk resonator with coupling gaps g_{emis} and g_{pump} for the emission and pump waveguide, respectively. The coupling gaps are determined by conducting parametric 3D eigenfrequency simulations with respect to g_{emis} and g_{pump} and targeting specific values for the external Q-factors (see next paragraph). It is important to note that ideally each mode is to be predominantly coupled to only one waveguide; some residual nonzero coupling to the other waveguide is merely an unavoidable side effect. Hence, the proposed cavity scheme does not resemble the standard add-drop filter configuration.

For the lasing mode, over-coupling with the emission waveguide ($Q_{e,\text{emis}}^{(m)} \ll Q_{\text{rad}}^{(m)}$) is highly favorable to increase P_{out} .^[41] Therefore, we opt for $Q_{e,\text{emis}} \approx 3000$ which can be obtained for $g_{\text{emis}} = 210 \text{ nm}$. Note that very low values of $Q_{e,\text{emis}}^{(m)}$ (≤ 1700) could prohibit the lasing process leading to $\Delta N_{\text{th}}^{(1)} > N_{\text{tot}}$. The coupling losses of the pump mode with the

Table 1. Electromagnetic parameters of the finally proposed Q-switched lasing element that feed the CMT framework. The geometric parameters of the proposed structure are $R = 1.4578 \mu\text{m}$, $h_{\text{SRN}} = 240 \text{ nm}$, $h_{\text{hBN}} = 70 \text{ nm}$, $w_{\text{emis}} = 180 \text{ nm}$, $w_{\text{pump}} = 80 \text{ nm}$, $g_{\text{emis}} = 210 \text{ nm}$, and $g_{\text{pump}} = 50 \text{ nm}$.

CMT parameters	Lasing mode [m]	Pump mode [p]
$\lambda_{c,0}^{(k)}$ [nm]	1 228	733.065
$Q_{\text{rad}}^{(k)}$	179 329	$\approx 10^9$
$\xi_g^{(k)}$ [V/C]	1.371×10^{16}	6.477×10^{15}
$\xi_{\text{eff}}^{(k)}$ [V/(Cm ²)]	2.067×10^{28}	1.295×10^{28}
$\xi_{\text{SA}}^{(k)}$ [V/C]	6.708×10^{15}	6.120×10^{14}
$Q_{\text{gr}}^{(k)}(0)$	2 040	34 416
$Q_{e,\text{emis}}^{(k)}$	2 994	$\approx 10^6$
$Q_{e,\text{pump}}^{(k)}$	10 130	3 715
$\lambda^{(k)}$ [nm]	–	733
$\lambda_{\text{ref}}^{(k)}$ [nm]	1 128	–

emission waveguide are totally negligible, $Q_{e,\text{emis}}^{(p)} \approx 10^6$. The pump mode, on the other hand, should be critically coupled with the pump waveguide in order to achieve $\eta_p \rightarrow 1$. For this purpose, the detuning term in Equation (14) should be compensated with the pump polarization-induced frequency shift (expressed through $\text{Re}\{\Delta\tilde{\omega}^{(p)}\}$) evaluated at the first lasing threshold. The latter is obtained by carefully selecting the wavelength of the input pump wave, $\lambda^{(p)}$, in order to fulfill the following equation:

$$\omega^{(p)} - \omega_{c,0}^{(p)} + \frac{\sigma_{31} \xi_g^{(p)} \omega_{c,0}^{(p)} [\omega_{31}^2 - (\omega^{(p)})^2]}{[\omega_{31}^2 - (\omega^{(p)})^2]^2 + (\omega^{(p)} \Gamma_{31})^2} \frac{\bar{N}_{\text{tot}} - \Delta \bar{N}_{21,\text{th}}^{(1)}}{2} = 0 \quad (15)$$

resulting in $\lambda^{(p)} = 733 \text{ nm}$ which is almost identical to $\lambda_{c,0}^{(p)}$ (cf. Table 1). Subsequently, the coupling losses, $1/\tau_{e,\text{pump}}^{(p)}$, should be equal to the absorption of the gain medium in the first lasing threshold, yielding

$$\frac{1}{\tau_{e,\text{pump}}^{(p)}} = \frac{\sigma_{31} \xi_g^{(p)} \omega_{c,0}^{(p)} \omega^{(p)} \Gamma_{31}}{[\omega_{31}^2 - (\omega^{(p)})^2]^2 + (\omega^{(p)} \Gamma_{31})^2} \frac{\bar{N}_{\text{tot}} - \Delta \bar{N}_{21,\text{th}}^{(1)}}{2} \quad (16)$$

From Equation (16) we get $Q_{e,\text{pump}}^{(p)} = 3 680$, which is obtained for $g_{\text{pump}} = 50 \text{ nm}$. Equation (15) and (16) are extracted from Equation (14) and (5b) in the adiabatic limit ($d^{(p)}/dt \rightarrow 0$) and by assuming that $\bar{N}_3 \ll \bar{N}_1, \bar{N}_2$; both approximations hold for the structure under study and the pump power levels we consider. In addition, we have set $\Delta \bar{N} = \Delta \bar{N}_{21,\text{th}}^{(1)}$, which ensures the fulfillment of the critical coupling condition at the first lasing threshold. The fact that the pump waveguide supports only the fundamental TM_{00} mode in the pump wavelength region implies that there are not any guided modes supported in the lasing wavelength region. Nonetheless, the lasing mode still couples to radiation modes of the pump waveguide, resulting in finite values of $Q_{e,\text{pump}}^{(m)}$, which needs to be as high as possible.

To attain high values of $Q_{e,\text{pump}}^{(m)}$, the lasing mode should be well confined in the disk resonator (see fourth design directive in Section 3). Indeed, by satisfying the relation $Q_{\text{rad}}^{(m)} > 100 000$, we obtain $Q_{e,\text{pump}}^{(m)} = 10 130$, which keeps the overall radiation losses of the lasing mode at acceptable levels (see also the Supporting Information, Section S2 for more details and results). The complete electromagnetic parameters of the finally proposed lasing element that feed the CMT framework are summarized in Table 1.

The patterning of the stack $\text{MoS}_2/\text{WSe}_2/\text{h-BN}/\text{graphene}$ and the precise positioning of it on top of the SRN disk resonator, might be technologically challenging for practical implementations of the proposed lasing element. In such cases, an unpatterned 2D material stack can be exploited on top of a silica-clad (thus planarized) SRN disk cavity. For the dimensions of the cavity designed previously, this alternative design could leave practically unaffected the relation between the ξ factors (first three design directives), but it would decrease the radiative Q-factor of the lasing mode ($Q_{\text{rad}}^{(m)} \approx 16 000$). To restore $Q_{\text{rad}}^{(m)}$ without affecting the ξ factors, the azimuthal order of the lasing

mode should increase in expense of higher radii values. More precisely, by exploiting the WGM with $m = 20$ ($R = 1.76 \mu\text{m}$) as the lasing mode, we obtain $Q_{\text{rad}}^{(m)} \approx 170\,000$. Therefore, the patterning of the 2D material stack is not necessary to achieve pulsed operation in the proposed lasing element, but it helps in making the structure more compact. In addition, in practical WGM cavities, the influence of the losses induced by impurities and sidewalls roughness of the SRN disk resonator should also be carefully considered. Fabrication-quality-related imperfections can be captured through an appropriate imaginary part in the SRN refractive index, leading to an additional channel of losses (measured by an appropriate quality factor) for both modes. The imaginary part of SRN can be obtained from experimentally measured propagation losses of fabricated SRNOI wire waveguides^[4] and used to estimate quality factors higher than 100 000. Such high values of the fabrication-related-losses quality factor would leave the overall lasing response practically unaffected, since the intrinsic quality factor of the lasing and pump modes would still be predominantly dictated by the losses of graphene and $\text{MoS}_2/\text{WSe}_2$, respectively. In addition, state-of-the-art electron beam lithography has made possible the fabrication of high-quality SRN nanodisk cavities^[55] rendering the proposed lasing structure readily feasible.

4. Laser Response

Having meticulously designed the Q-switched lasing element in Section 3, we now assess its CW and pulsed performance. For this purpose, the electromagnetic parameters of Table 1 are introduced in the CMT framework (Equation (5), (8), (13) and (14)) that has been developed in Section 2 and system of equations is numerically solved.

4.1. Continuous-Wave Operation

Initially, we study the CW response of the lasing element by artificially switching-off the graphene SA effect ($E_{\text{sat}} \rightarrow \infty$ in Equation (11)). The light-light curve is depicted in **Figure 3a**. The evaluated pump power threshold is only $P_{p,\text{th}} = 24.2 \mu\text{W}$, due to the highly efficient pumping scheme with guided light and the fulfillment of the critical coupling condition for the pump mode. As a remark, we note that the calculated threshold is in good agreement with that of the experimental work.^[30] Above the lasing threshold the light-light curve is linear and the lasing element is characterized by a high total quantum efficiency of $\approx 27\%$. This is a direct consequence of the advantageous pumping and out-coupling emission schemes we have employed through the double-access configuration with dissimilar waveguides, constituting one of the novelties of our work that is important in pushing integrated nanophotonic laser sources towards realizing their full potential. Nonetheless, the overall quantum efficiency of the laser is limited to $\approx 27\%$ due to 1) the presence of resistive and radiation losses in the lasing mode, 2) the incoherent radiative (spontaneous emission) and nonradiative recombination processes in level 2, and 3) the considerable quantum defect of $1 - \omega_{21}/\omega_{31} = 0.34$. The absorption efficiency and the pump transmission coefficient ($P_{p,\text{trans}}/P_p$) are

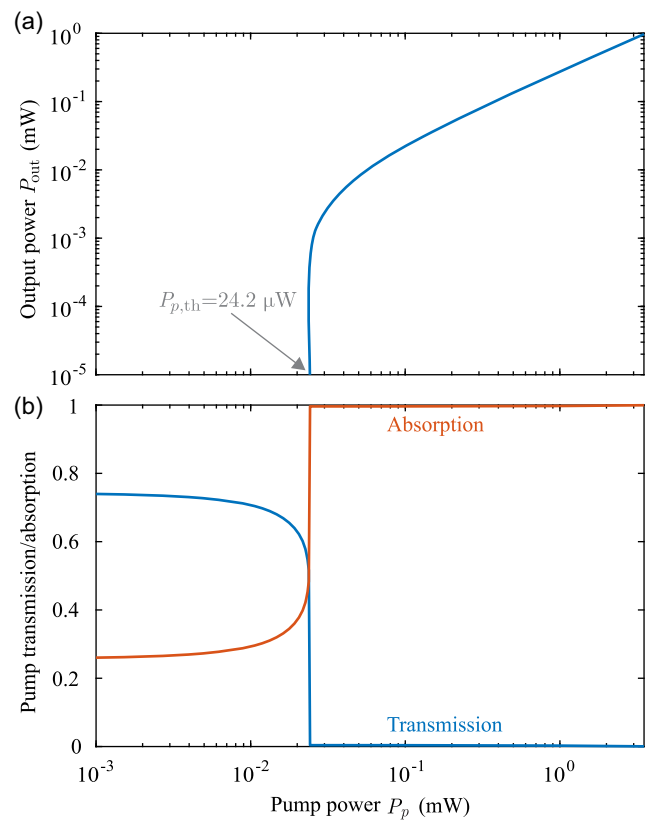


Figure 3. Continuous-wave operation of the proposed lasing element evaluated in the absence of SA by setting $E_{\text{sat}} \rightarrow \infty$ in Equation (11). a) Output power P_{out} as a function of the pump power P_p . The lasing threshold is $P_{p,\text{th}} = 24.2 \mu\text{W}$. b) Absorption efficiency, η_p , and pump transmission coefficient, $P_{p,\text{trans}}/P_p$, as a function of the pump power.

depicted in Figure 3b. For pump power levels above the lasing threshold, the critical coupling condition is satisfied resulting in $\eta_p = 1$ and the transmitted pump wave is zeroed-out. This, however, is not the case below the (first) lasing threshold ($P_p < P_{p,\text{th}}$) where the critical coupling condition is not met (since now $\Delta\bar{N} \neq \Delta\bar{N}_{21,\text{th}}^{(1)}$) and the absorption efficiency is sub-optimal. The results presented in Figure 3 cover pump powers from $1 \mu\text{W}$ up to 3.5mW , a range which attracts the most practical interest and the heat generated by the input pump wave remains at acceptable levels (see the discussion below and the Supporting Information, Section S4). As the pump power approaches $P_p \approx 20 \text{mW}$, the pump absorption process is quenched due to Pauli blocking, resulting in saturation of the output power (see the Supporting Information, Section S3.i).

4.2. Pulsed Operation

The presence of graphene SA leads the cavity to an instability just above the lasing threshold, giving rise to pulsed operation originating from the Q-switching mechanism. In **Figure 4** we present the response of the lasing element for $P_p = 2 \text{mW}$. Figure 4a depicts the temporal evolution of the output power, P_{out} .

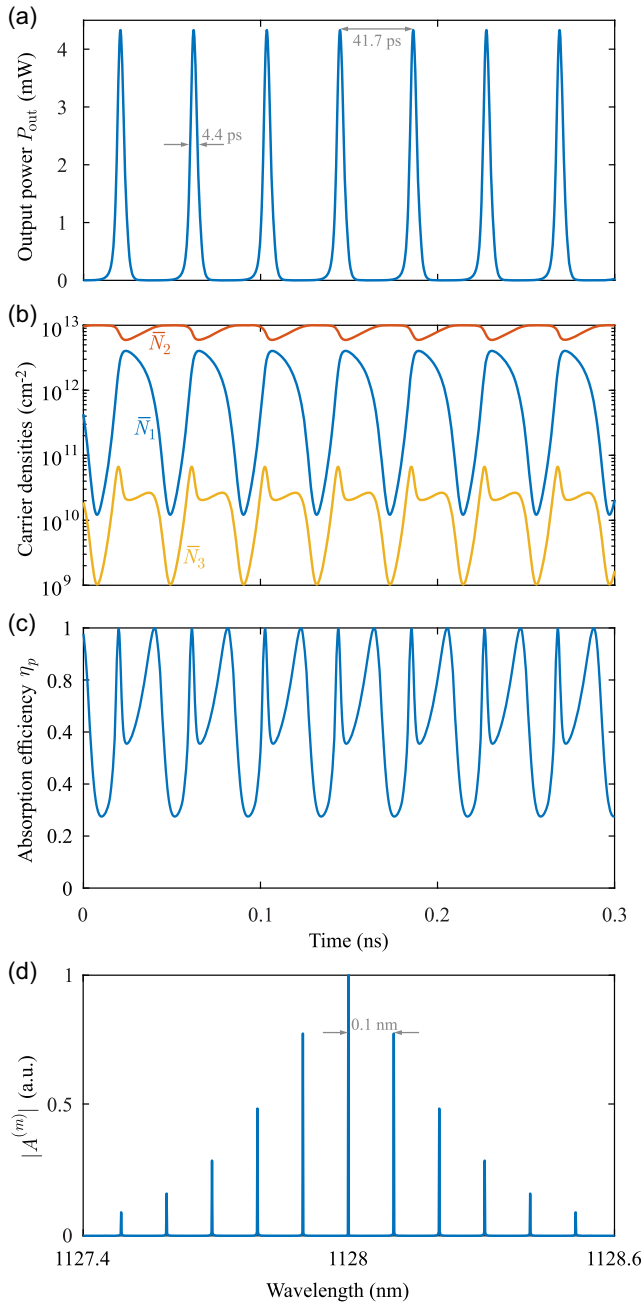


Figure 4. Q-switched operation of the proposed lasing element when the pump power is $P_p = 2$ mW. Temporal evolution of a) output power, b) carrier densities in the three levels of the gain medium, and c) absorption efficiency of the pump mode. d) Optical spectrum of the lasing mode cavity amplitude. The annotated wavelength spacing corresponds to the repetition rate of the pulsetrain output.

The Q-switched pulse train is characterized by high peak power of $P_{\text{out}}^{\text{peak}} = 4.33$ mW, short pulse duration with full-width at half maximum (FWHM) equal to $\text{FWHM} = 4.43$ ps, and high repetition rate of $R_r = 24$ GHz, corresponding to a repetition period of 41.7 ps. The temporal evolution of the spatially-averaged carrier density for the three levels of the gain medium is presented

in Figure 4b; note that the y-axis is in logarithmic scale. Initially, the input pump power creates a practically complete population inversion, $\Delta\bar{N}_{21} \approx N_{\text{tot}}$, which initiates the development of a Q-switched pulse. Thereafter, the emission of such a high peak power pulse results in the quick depletion of the carriers from level 2 to level 1, as it is indicated by the dip (peak) in the \bar{N}_2 (\bar{N}_1) curve. The resulting population inversion drops below the first lasing threshold $\Delta\bar{N}_{21}^{(1)}$, preventing, consequently, the lasing process. The population inversion is then slowly recovered under the influence of the pump mode and the aforementioned cycle repeats. The surface carrier density in level 3, \bar{N}_3 , is two orders of magnitude lower than \bar{N}_1 and \bar{N}_2 due to the practically instantaneous relaxation from level 3 to level 2. The temporal evolution of \bar{N}_3 , however, is different than that of \bar{N}_1 and \bar{N}_2 , experiencing two peaks during the emission of an individual Q-switched pulse. This behavior is consistent with the temporal evolution of the absorption (Figure 4c) varying from 0.28 to 1. This large variation of η_p during the Q-switching process reveals that the lasing and pump modes are highly entangled and jointly dictate the carrier dynamics of the gain medium. As it has become obvious from the previous discussion, during the development of an individual Q-switched pulse, the population inversion becomes twice equal to $\Delta\bar{N}_{21}^{(1)}$; before and just after the emission of the pulse. Therefore, the critical coupling condition is met at these two instances resulting in $\eta_p = 1$. In effect, this leads to a maximum of photogenerated carriers in level 3, thus, explaining the two peaks of \bar{N}_3 curve in a single Q-switched period.

The optical spectrum of the lasing mode cavity amplitude, $a^{(m)}$, is depicted in Figure 4d, consisting of equidistant and progressively decreasing peaks around the central lasing wavelength of 1128 nm. The peak distance is 0.1 nm which corresponds to the repetition rate of $R_r = 24$ GHz. Note that the central lasing wavelength is equal to the central emission wavelength λ_{21} , as a result of the resonance wavelength of the lasing mode being $\lambda_{c,0}^{(m)} = \lambda_{21}$ (see also the Supporting Information, Section S3.ii for more results).

Q-switched operation can be obtained for a wide range of pump power levels starting from the lasing threshold. When increasing the pump power above 3.5 mW, the individual pulses have closely approached each other and overlap; as a result, in such cases the extinction ratio receives finite values. For $P_p > 5.2$ mW the Q-switched operation stops completely and the lasing element operates in CW. Given the above, the pump power levels from 24.2 μW to 3.5 mW attract the main interest for practical applications. For these P_p values, the response of the Q-switched element is qualitatively the same as the one presented in Figure 4. In Figure 5, we examine how the quantitative characteristics of the Q-switched pulse train varies as a function of P_p in the said range. The output peak power $P_{\text{out}}^{\text{peak}}$ (Figure 5a) rises from 79 μW to 6.08 mW. It is noteworthy that we can achieve $P_{\text{out}}^{\text{peak}} = 1$ mW for just 45 μW of (CW) pump power. The FWHM of the pulses (Figure 5a) is in the ps time scale (same order of magnitude with $\tau_{\rho}^{(m)}$) and decreases gradually from 6.35 ps for $P_p = 45$ μW to its lowest values of 4.35 ps for

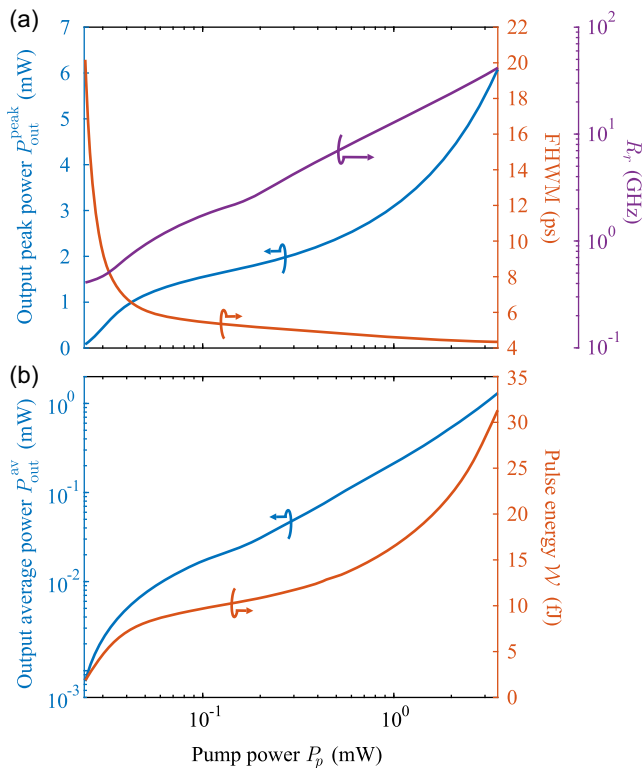


Figure 5. Metrics of the obtained Q-switched pulse trains as a function of the pump power from the lasing threshold (24.2 μ W) up to 3.5 mW where an infinite extinction ratio can be obtained. a) Output peak power, full-width at half maximum, and repetition rate and b) output average power and pulse energy.

$P_p = 3.5$ mW. The repetition rate increases almost linearly (Figure 5a) and spans a range of two orders of magnitude: from 0.41 to 42 GHz. By increasing P_p , the initial population inversion in the gain medium is larger and requires more energy from the lasing mode to deplete it, which consequently results in greater peak power and shorter duration output pulses. Concurrently, with greater values of P_p the population inversion recovers faster after the emission of an individual Q-switched pulse leading to higher repetition rates, thus justifying the trends followed by P_{out}^{peak} , FWHM, and R_r with P_p . The evaluated performance metrics of the proposed Q-switched laser are in quite good agreement with the experimental work of ref. [7]. Despite the differences in the employed cavity as well as the SA and gain media (thus leading to quite different pump and lasing wavelengths) between the two works, this agreement strengthens our belief that our simulated results are realistic and could be experimentally verified.

In Figure 5b, we plot the average output power P_{out}^{av} versus P_p , which rises from 0.76 μ W up to 1.3 mW (for 3.5 mW pump power) indicating a total quantum efficiency for the pulsed laser of 37%, increased with respect to that derived in Section 4.1 for CW operation. The pulse energy, W , is also presented in Figure 5b. It experiences an almost 20-fold increase in the examined pump power range. The evolution of W is practically identical to that of P_{out}^{peak} , since the increase in P_{out}^{peak} is stronger than the

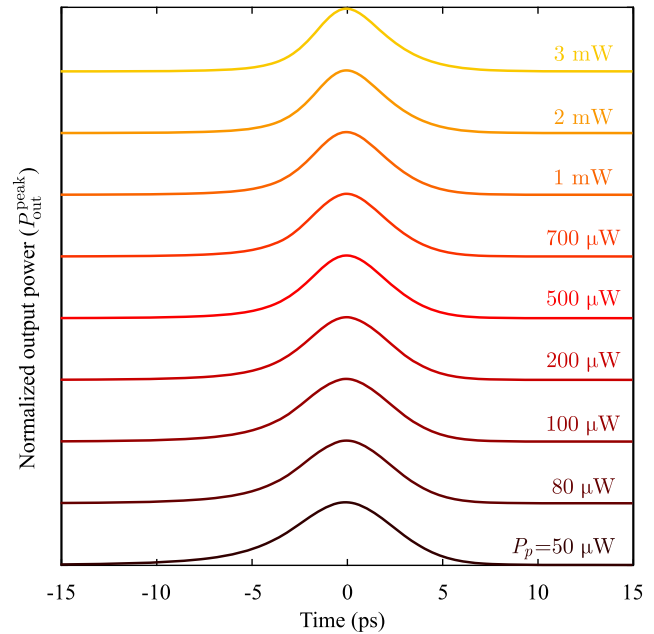


Figure 6. Dependence of lineshape of the individual Q-switched pulses with pump power. The pulses are quite symmetric. Slightly longer leading edges are observed for low values of P_p , whereas slightly longer trailing edges for higher values of P_p .

decrease in FWHM. Finally, the dependence of the lineshape of individual Q-switched pulses with pump power is illustrated in Figure 6. The individual Q-switched pulses are characterized by highly-symmetric lineshapes regardless of P_p , which is attributed to the fact that the saturable and nonsaturable losses of the lasing mode are equally dominant. This can be verified by comparing $Q_{e,emis}^{(m)}$ and $Q_{gr}^{(m)}(0)$ in Table 1. In addition, we can observe a transition from pulses with slightly longer leading edges for lower values of P_p , to pulses with longer trailing edges for higher values of P_p , which suggests the non-negligible role of the pump mode on the carrier dynamics of the gain medium and, hence, on P_{out} .

It is also important to discuss the thermal stability of the proposed lasing element, since heating effects induced by strong light absorption could hamper the lasing process and damage the nanophotonic laser. For this purpose, we conduct heat transfer simulations using COMSOL Multiphysics aiming at examining the heat removal capability of the proposed lasing element and evaluate the highest possible lattice temperature increase that could occur during its operation. We assume that the heat sources in our structure are the fraction of the pump power absorbed by the TMD bilayer that is not offered to the lasing mode, and the entire energy of the lasing mode that is absorbed by the graphene monolayer. Note that since SRN, h-BN, and SiO₂ are all transparent at both lasing and pump wavelengths, they do not contribute to generating heat. The simulations were conducted according to ref. [49]. For $P_p = 3.5$ mW (the highest pump power level examined previously), we obtain the maximum temperature rise of $\Delta T = 87.7$ K, which can be considered acceptable. In addition, the maximum pump power density in the TMD bilayer is calculated to be ≈ 362 kWcm⁻², which is

two orders of magnitude lower than the optical damage limit of TMDs ($\approx 10 \text{ MWcm}^{-2}$)^[56] and close to practical pump power irradiances used in the literature.^[26] Note that the optical damage limit of graphene is three orders of magnitude greater ($\approx 1 \text{ GWcm}^{-2}$)^[11] (see also the Supporting Information, Section S4 for more details and results).

5. Conclusion

To recapitulate, we have proposed thoroughly designed and assessed the performance of an integrated nanophotonic passive Q-switched lasing element in the NIR, where the optically pumped gain is provided by an MoS₂/WSe₂ TMD hetero-bilayer and the ultrafast SA effect by a graphene monolayer. The laser is based on an SRNOI disk resonator with the 2D gain and SA media residing on top and separated by a finite-height layer of h-BN. The optical pumping is conducted with guided light. By ensuring high absorption efficiency and satisfying a critical coupling condition, an ultralow lasing threshold of just 24.2 μW has been obtained. The geometric parameters of the structure have been determined following a meticulous design process in order to achieve the appropriate light–matter interaction between each mode and the 2D gain and SA media, as well as the suitable coupling with the double bus waveguide scheme we exploit. To numerically evaluate the overall response of the structure, we have developed a CMT framework fed by linear FEM simulations, which has been rigorously extracted from the semiclassical Maxwell–Bloch equations utilizing only first-order perturbation theory and the standard slowly varying envelope and rotating wave approximations. The lasing and pump transitions are explicitly treated through induced polarization fields and the carrier dynamics are described by carrier rate equations. The framework is general and can be employed for any “class C” laser.

Overall, the proposed structure is capable of delivering pulsed light with high total quantum efficiency inside an integrated bus waveguide with mW peak power, ps duration, and repetition rates up to tens of GHz, while requiring sub-mW pump powers (CW). Importantly, the repetition rate can be tuned by varying the pump power level. These highly favorable properties, in combination with the compact footprint ($< 2 \times 2 \mu\text{m}^2$) and the SOI compatibility, constitute our proposed Q-switched lasing element highly favorable for a wide variety of modern communication applications in the NIR.

Supporting Information

Supporting Information is available from the Wiley Online Library or from the author.

Acknowledgements

The research work was supported by the Hellenic Foundation for Research and Innovation (H.F.R.I.) under the “First Call for H.F.R.I. Research Projects to support Faculty members and Researchers and the procurement of high-cost research equipment grant” (Project Number: HFRI-FM17-2086).

Conflict of Interest

The authors declare no conflict of interest.

Data Availability Statement

The data that support the findings of this study are available from the corresponding author upon reasonable request.

Keywords

coupled-mode theory, transition-metal dichalcogenide bilayer, graphene saturable absorber, microdisk resonator, pulsed lasing

Received: August 25, 2023

Revised: January 24, 2024

Published online:

- [1] J. K. Doylend, A. P. Knights, *Laser Photonics Rev.* **2012**, *6*, 504.
- [2] G. Sinatkas, T. Christopoulos, O. Tsilipakos, E. E. Kriezis, *J. Appl. Phys.* **2021**, *130*, 1.
- [3] D. T. H. Tan, K. J. A. Ooi, D. K. T. Ng, *Photonics Res.* **2018**, *6*, B50.
- [4] T. Wang, D. K. Ng, S. K. Ng, Y. T. Toh, A. K. Chee, G. F. Chen, Q. Wang, D. T. Tan, *Laser Photonics Rev.* **2015**, *9*, 498.
- [5] B. U. Sohn, J. W. Choi, D. K. Ng, D. T. Tan, *Sci. Rep.* **2019**, *9*, 1.
- [6] D. S. Liu, J. Wu, H. Xu, Z. Wang, *Adv. Mater.* **2021**, *33*, 1.
- [7] Y. Yu, W. Xue, E. Semanova, K. Yvind, J. Mork, *Nat. Photonics* **2017**, *11*, 81.
- [8] U. Keller, K. J. Weingarten, F. X. Kärtner, D. Kopf, B. Braun, I. D. Jung, R. Fluck, C. Hönninger, N. Matuschek, J. Aus Der Au, *IEEE J. Sel. Top. Quantum Electron.* **1996**, *2*, 435.
- [9] F. X. Kaertner, L. R. Brovelli, D. Kopf, M. Kamp, I. G. Calasso, U. Keller, *Opt. Eng.* **1995**, *34*, 2024.
- [10] Y. N. Zhang, Z. Y. Song, D. Qiao, X. H. Li, Z. Guang, S. P. Li, L. B. Zhou, X. H. Chen, *Nanotechnology* **2022**, *33*, 82003.
- [11] F. Zhang, S. Han, Y. Liu, Z. Wang, X. Xu, *Appl. Phys. Lett.* **2015**, *106*, 1.
- [12] A. Marini, J. D. Cox, F. J. García De Abajo, *Phys. Rev. B* **2017**, *95*, 1.
- [13] Q. Bao, H. Zhang, Y. Wang, Z. Ni, Y. Yan, Z. X. Shen, K. P. Loh, D. Y. Tang, *Adv. Funct. Mater.* **2009**, *19*, 3077.
- [14] S. A. Mikhailov, *Phys. Rev. B* **2019**, *100*, 115416.
- [15] P. Demongodin, H. El Dirani, J. Lhuillier, R. Crochemore, M. Kemiche, T. Wood, S. Callard, P. Rojo-Romeo, C. Sciancalepore, C. Grillet, C. Monat, *APL Photonics* **2019**, *4*, 7.
- [16] K. Alexander, N. A. Savostianova, S. A. Mikhailov, D. Van Thourhout, B. Kuyken, *ACS Photonics* **2018**, *5*, 4944.
- [17] A. Ptilakis, E. E. Kriezis, *J. Opt. Soc. Am. B* **2022**, *39*, 2723.
- [18] F. Lohof, A. Steinhoff, M. Florian, M. Lorke, D. Erben, F. Jahnke, C. Gies, *Nano Lett.* **2019**, *19*, 210.
- [19] M. Palumbo, M. Bernardi, J. C. Grossman, *Nano Lett.* **2015**, *15*, 2794.
- [20] G. Moody, C. Kavar Dass, K. Hao, C. H. Chen, L. J. Li, A. Singh, K. Tran, G. Clark, X. Xu, G. Berghäuser, E. Malic, A. Knorr, X. Li, *Nat. Commun.* **2015**, *6*, 8315.
- [21] M. Selig, G. Berghäuser, M. Richter, R. Bratschitsch, A. Knorr, E. Malic, *2D Mater.* **2018**, *5*, 3.
- [22] H. L. Liu, C. C. Shen, S. H. Su, C. L. Hsu, M. Y. Li, L. J. Li, *Appl. Phys. Lett.* **2014**, *105*, 20.
- [23] C. Hsu, R. Frisenda, R. Schmidt, A. Arora, S. M. de Vasconcellos, R. Bratschitsch, H. S. van der Zant, A. Castellanos-Gomez, *Adv. Opt. Mater.* **2019**, *7*, 13.
- [24] C. Jin, E. Y. Ma, O. Karni, E. C. Regan, F. Wang, T. F. Heinz, *Nat. Nanotechnol.* **2018**, *13*, 994.

- [25] Y. Jiang, S. Chen, W. Zheng, B. Zheng, A. Pan, *Light: Sci. Appl.* **2021**, *10*, 1.
- [26] P. Nagler, G. Plechinger, M. V. Ballottin, A. Mitioglu, S. Meier, N. Paradiso, C. Strunk, A. Chernikov, P. C. Christianen, C. Schüller, T. Korn, *2D Mater.* **2017**, *4*, 2.
- [27] J. S. Ross, P. Rivera, J. Schaibley, E. Lee-Wong, H. Yu, T. Taniguchi, K. Watanabe, J. Yan, D. Mandrus, D. Cobden, W. Yao, X. Xu, *Nano Lett.* **2017**, *17*, 638.
- [28] A. Y. Joe, L. A. Jauregui, K. Pistunova, A. M. Mier Valdivia, Z. Lu, D. S. Wild, G. Scuri, K. De Greve, R. J. Gelly, Y. Zhou, J. Sung, A. Sushko, T. Taniguchi, K. Watanabe, D. Smirnov, M. D. Lukin, H. Park, P. Kim, *Phys. Rev. B* **2021**, *103*, 16.
- [29] O. Karni, E. Barré, S. C. Lau, R. Gillen, E. Y. Ma, B. Kim, K. Watanabe, T. Taniguchi, J. Maultzsch, K. Barmak, R. H. Page, T. F. Heinz, *Phys. Rev. Lett.* **2019**, *123*, 24.
- [30] Y. Liu, H. Fang, A. Rasmita, Y. Zhou, J. Li, T. Yu, Q. Xiong, N. Zheludev, J. Liu, W. Gao, *Sci. Adv.* **2019**, *5*, 4.
- [31] J. D. Caldwell, I. Aharonovich, G. Cassabois, J. H. Edgar, B. Gil, D. N. Basov, *Nat. Rev. Mater.* **2019**, *4*, 552.
- [32] Y. Rah, Y. Jin, S. Kim, K. Yu, *Opt. Lett.* **2019**, *44*, 3797.
- [33] R. Khelifa, P. Back, N. Flöry, S. Nashashibi, K. Malchow, T. Taniguchi, K. Watanabe, A. Jain, L. Novotny, *Nano Lett.* **2020**, *20*, 6155.
- [34] S. Kim, J. E. Fröch, J. Christian, M. Straw, J. Bishop, D. Totonjian, K. Watanabe, T. Taniguchi, M. Toth, I. Aharonovich, *Nat. Commun.* **2018**, *9*, 1.
- [35] W. Suh, Z. Wang, S. Fan, *IEEE J. Quantum Electron.* **2004**, *40*, 1511.
- [36] S.-L. Chua, Y. Chong, A. D. Stone, M. Soljacic, J. Bravo-Abad, *Opt. Express* **2011**, *19*, 1539.
- [37] O. Tsilipakos, T. Christopoulos, E. E. Kriezis, *J. Lightwave Technol.* **2016**, *34*, 1333.
- [38] T. Christopoulos, O. Tsilipakos, N. Grivas, E. E. Kriezis, *Phys. Rev. E* **2016**, *94*, 1.
- [39] T. Christopoulos, O. Tsilipakos, G. Sinatkas, E. E. Kriezis, *Phys. Rev. B* **2018**, *98*, 1.
- [40] G. Nousios, T. Christopoulos, O. Tsilipakos, E. E. Kriezis, *J. Appl. Phys.* **2022**, *131*, 5.
- [41] G. Nousios, T. Christopoulos, O. Tsilipakos, E. E. Kriezis, *Phys. Rev. Appl.* **2023**, *19*, 6.
- [42] A. E. Siegman, *Lasers*, University Science Books, New York **1986**.
- [43] A. Fang, T. Koschny, C. M. Soukoulis, *J. Opt. A: Pure Appl. Opt.* **2010**, *12*, 2.
- [44] C. Fietz, C. Soukoulis, *Opt. Express* **2012**, *20*, 11548.
- [45] A. Cerjan, Y. D. Chong, A. D. Stone, *Opt. Express* **2015**, *23*, 6455.
- [46] D. Chatzidimitriou, A. Ptilakis, E. E. Kriezis, *J. Appl. Phys.* **2015**, *118*, 2.
- [47] V. G. Ataloglou, T. Christopoulos, E. E. Kriezis, *Phys. Rev. A* **2018**, *97*, 6.
- [48] J. Bravo-Abad, S. Fan, S. G. Johnson, J. D. Joannopoulos, M. Soljačić, *J. Lightwave Technol.* **2007**, *25*, 2539.
- [49] O. Tsilipakos, T. V. Yioultsis, E. E. Kriezis, *J. Appl. Phys.* **2009**, *106*, 1.
- [50] P. Hamel, S. Haddadi, F. Raineri, P. Monnier, G. Beaudoin, I. Sagnes, A. Levenson, A. M. Yacomotti, *Nat. Photonics* **2015**, *9*, 311.
- [51] Y. Yu, A. Sakanas, A. R. Zali, E. Semenova, K. Yvind, J. Mørk, *Nat. Photonics* **2021**, *15*, 758.
- [52] L. A. Coldren, S. W. Corzine, M. L. Mašanović, *Diode Lasers and Photonic Integrated Circuits*, Wiley, Hoboken, NJ **2012**.
- [53] S.-H. Chang, A. Taflove, *Opt. Express* **2004**, *12*, 3827.
- [54] N. Vermeulen, D. Castelló-Lurbe, M. Khoder, I. Pasternak, A. Krajewska, T. Ciuk, W. Strupinski, J. L. Cheng, H. Thienpont, J. Van Erps, *Nat. Commun.* **2018**, *9*, 1.
- [55] C.-S. Park, I. Koirala, S. Gao, V. R. Shrestha, S.-S. Lee, D.-Y. Choi, *Opt. Express* **2019**, *27*, 667.
- [56] A. Castellanos-Gomez, M. Barkelid, A. M. Goossens, V. E. Calado, H. S. Van Der Zant, G. A. Steele, *Nano Lett.* **2012**, *12*, 3187.